Monthly Notices
of the
ROYAL ASTRONOMICAL SOCIETY

MNRAS **475,** 2496–2511 (2018)
Advance Access publication 2017 December 27

doi:10.1093/mnras/stx3340

Mapping low-frequency carbon radio recombination lines towards Cassiopeia A at 340, 148, 54, and 43 MHz

P. Salas,[1]★ J. B. R. Oonk,[1,2] R. J. van Weeren,[3] M. G. Wolfire,[4] K. L. Emig,[1] M. C. Toribio,[1] H. J. A. Röttgering[1] and A. G. G. M. Tielens[1]

[1]*Leiden Observatory, Leiden University, PO Box 9513, NL-2300 RA Leiden, the Netherlands*
[2]*Netherlands Institute for Radio Astronomy (ASTRON), Postbus 2, NL-7990 AA Dwingeloo, the Netherlands*
[3]*Harvard-Smithsonian Center for Astrophysics, 60 Garden Street, Cambridge, MA 02138, USA*
[4]*Department of Astronomy, University of Maryland, College Park, MD 20742, USA*

Accepted 2017 December 21. Received 2017 December 21; in original form 2017 September 10

ABSTRACT

Quantitative understanding of the interstellar medium requires knowledge of its physical conditions. Low-frequency carbon radio recombination lines (CRRLs) trace cold interstellar gas and can be used to determine its physical conditions (e.g. electron temperature and density). In this work, we present spatially resolved observations of the low-frequency ($\leq$390 MHz) CRRLs centred around C268α, C357α, C494α, and C539α towards Cassiopeia A on scales of $\leq$1.2 pc. We compare the spatial distribution of CRRLs with other interstellar medium tracers. This comparison reveals a spatial offset between the peak of the CRRLs and other tracers, which is very characteristic for photodissociation regions and that we take as evidence for CRRLs being preferentially detected from the surfaces of molecular clouds. Using the CRRLs, we constrain the gas electron temperature and density. These constraints on the gas conditions suggest variations of less than a factor of 2 in pressure over $\sim$1 pc scales, and an average hydrogen density of 200–470 cm^{-3}. From the electron temperature and density maps, we also constrain the ionized carbon emission measure, column density, and path length. Based on these, the hydrogen column density is larger than 10^{22} cm^{-2}, with a peak of $\sim 4 \times 10^{22}$ cm^{-2} towards the south of Cassiopeia A. Towards the southern peak, the line-of-sight length is $\sim$40 pc over a $\sim$2 pc wide structure, which implies that the gas is a thin surface layer on a large (molecular) cloud that is only partially intersected by Cassiopeia A. These observations highlight the utility of CRRLs as tracers of low-density extended H I and CO-dark gas halo's around molecular clouds.

Key words: ISM: clouds – ISM: individual objects: Cassiopeia A – radio lines: ISM.

1 INTRODUCTION

Molecular hydrogen, the material that fuels star formation, is formed out of atomic hydrogen (e.g. Cazaux & Tielens 2004). This is clear in the interstellar medium (ISM), where we observe that molecular gas is embedded in atomic hydrogen (e.g. Andersson, Wannier & Morris 1991; Williams & Maddalena 1996; Moriarty-Schieven & Wannier 1997; Fukui et al. 2009; Pascucci et al. 2015). Despite the clear association between these two gas compositions, the exact details of what is this atomic envelope are not clear (e.g. Blitz & Williams 1999; Hollenbach & Tielens 1999). In order to understand better the relation between mostly molecular dense gas and mostly atomic diffuse gas, a larger sample of gas in this transition regime is required, along accurate estimates of its temperature and density.

A way in which we can study the cold atomic gas in the envelopes of molecular clouds is through observations of low frequency ($\nu \lesssim$ 1 GHz) carbon radio recombination lines (CRRLs; e.g. Gordon & Sorochenko 2009). The population of carbon ions recombining to a given principal quantum number, n, is determined by the gas density, temperature, and radiation field, as well as the atomic physics involved (e.g. Shaver 1975; Watson, Western & Christensen 1980; Salgado et al. 2017a). Thus, we can determine the gas physical conditions by comparing the observed properties of CRRLs at different frequencies with model predictions (e.g. Payne, Anantharamaiah & Erickson 1989; Kantharia, Anantharamaiah & Payne 1998; Oonk et al. 2017). Using this method, it has been determined that CRRLs trace cold ($T \sim 100$ K) diffuse gas ($n_{\rm H} \sim 100$ cm^{-3}, e.g. Konovalenko 1984; Ershov et al. 1987; Sorochenko & Walmsley

★ E-mail: psalas@strw.leidenuniv.nl

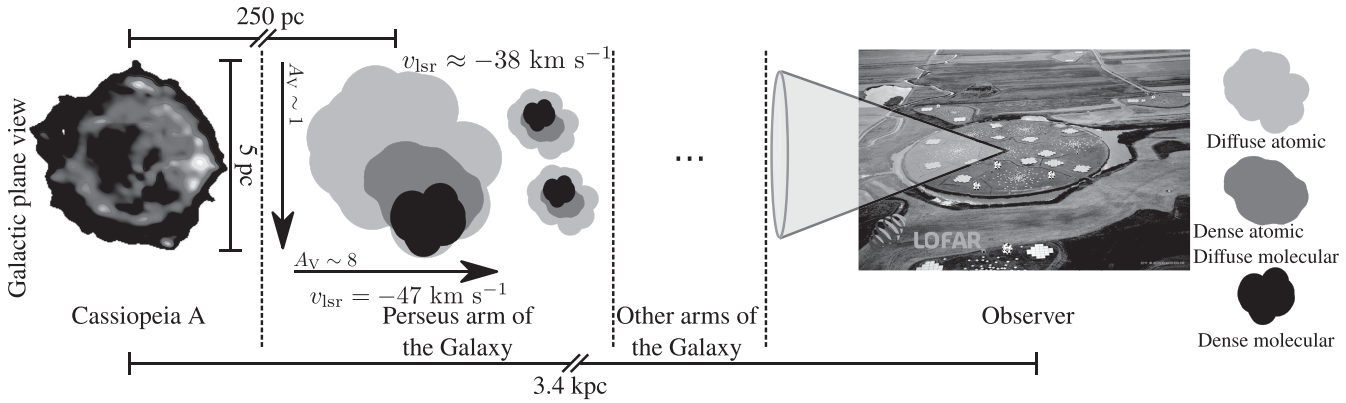

Figure 1. Cartoon depicting the geometry of the studied gas relative to Cassiopeia A and the observer. The gas studied in this work is part of the Perseus arm of the Galaxy and does not show signs of being related to the supernova remnant. The dense molecular gas peaks to the south of Cas A, as shown by continuum observations in the far-infrared (De Looze et al. 2017) and CO lines (e.g. Liszt & Lucas 1999; Kilpatrick, Bieging & Rieke 2014). Here we only illustrate the gas over the face of Cas A as our RRL observations do not trace gas outside the face of Cas A.

1991; Payne, Anantharamaiah & Erickson 1994; Kantharia, Anantharamaiah & Payne 1998; Roshi & Kantharia 2011; Oonk et al. 2017) in the Galaxy. These physical conditions are similar to those found from observations of atomic hydrogen associated with molecular clouds, either using self-absorption features [H I self absorption (HISA); e.g. Gibson 2002; Kavars et al. 2003, 2005; Kerton 2005; Moss et al. 2012] or absorption measurements against bright background continuum sources [H I continuum absorption (HICA); e.g. Dickey et al. 2009; Stanimirović et al. 2014; Bihr et al. 2015].

Most of our understanding of low-frequency CRRLs in the Galaxy comes from studies where the spatial resolution is coarse (e.g. $\theta_{\rm HPBW} \gtrsim 30$ arcmin Anantharamaiah, Payne & Erickson 1988; Erickson, McConnell & Anantharamaiah 1995; Kantharia & Anantharamaiah 2001; Roshi, Kantharia & Anantharamaiah 2002). This has hindered a spatially resolved identification of which components of the ISM do low-frequency CRRLs preferentially trace, such as the outskirts of H II regions, diffuse C II clouds, and/or the envelopes of molecular clouds. A notable exception to this limitation is the line of sight towards the supernova remnant Cassiopeia A (Cas A). Along this line of sight, the bright background continuum (relative to the diffuse synchrotron emission from the Milky Way) enables RRL studies with an effective resolution comparable to the size of Cas A (diameter of 6 arcmin at 64 MHz, e.g. Oonk et al. 2017). Additionally, the large gas column density in the intervening ISM has allowed a direct detection of CRRLs with a spatial resolution smaller than the size of Cas A (Anantharamaiah et al. 1994; Kantharia et al. 1998; Asgekar et al. 2013). From these observations, we know that the optical depth of the CRRLs associated with gas in the Perseus arm increases towards the south of Cas A (Anantharamaiah et al. 1994; Kantharia et al. 1998), peaking against its western hot spot (Asgekar et al. 2013).

Besides low-frequency CRRLs, the line of sight towards Cas A has been the target of numerous studies of the ISM (e.g. Davies & Matthews 1972; Mebold & Hills 1975; Troland, Crutcher & Heiles 1985; Bieging & Crutcher 1986; Wilson et al. 1993; Liszt & Lucas 1999; De Looze et al. 2017). Given that Cas A is located on the far side of the Perseus arm of the Galaxy (at a distance of 3.4 kpc from the observer Reed et al. 1995), most of the Perseus arm gas lies between the observed and the background source (e.g. Troland et al. 1985). Additionally, the distance between Cas A and the gas in the Perseus arms is large enough that they should be unrelated (Xu et al. 2006; Sorochenko & Smirnov 2010; Choi et al. 2014; Salas et al. 2017). The spatial distribution of the atomic gas towards Cas A shows that it completely covers the face of Cas A, as revealed by observations of the 21 cm line of H I in absorption against Cas A (e.g. Bieging, Goss & Wilcots 1991; Schwarz, Goss & Kalberla 1997). However, the saturation of the 21 cm H I line profiles makes it difficult to identify small-scale structure. Observations of other tracers have revealed the presence of gas with a large column density over the southern half of Cas A, with a visual extinction in the range of $A_V \sim 4$–10 (e.g. Troland et al. 1985; Hwang & Laming 2012; De Looze et al. 2017). A cartoon illustrating the distribution of the gas relative to Cas A and the observer is shown in Fig. 1.

The larger optical depth of CRRLs towards the south of Cas A (Anantharamaiah et al. 1994; Kantharia et al. 1998), where CO emission is readily detected, provides evidence, for the association of low frequency CRRLs with cold atomic or diffuse molecular envelopes of molecular clouds (e.g. Andersson et al. 1991). Another argument in favour of this association comes from the gas temperature and density as traced by low-frequency CRRLs. Using spatially unresolved observations of CRRLs, Oonk et al. (2017) derived a gas electron temperature of 85 K and a density of $\sim$280 cm^{-3}, in between those of cold molecular and diffuse atomic gas. A step forward in this direction would be to extend this spatial comparison to the gas physical conditions, which was not possible previously due to the lack of frequency coverage.

In this work, we present CRRL emission and absorption cubes centred around the C268α, C357α, C494α, and C539α lines with a resolution of 70 arcsec (1.2 pc at the distance of Cas A). With these cubes, we aim to study the relation between the gas traced by low-frequency CRRLs and other tracers of cold gas such as cold atomic gas traced by the 21 cm line of H I in absorption and molecular gas as traced by CO lines in the millimetre. We perform this comparison both spatially and in terms of the physical conditions as derived from two sets of lines: one containing the CRRLs and the second the molecular lines.

2 OBSERVATIONS AND DATA REDUCTION

Here, we describe the data reduction of the low frequency array (LOFAR; van Haarlem et al. 2013) high band antenna (HBA) observations presented in this work, as well as further processing steps applied to the previously published observations used. For the

Table 1. Selected observations towards Cas A.

Line or band	Telescope	Velocity resolution (km s^{-1})	Spatial resolution[a]	Reference
C268α	WSRT	0.6	70 arcsec × 70 arcsec 0°	This work
C357α	LOFAR HBA	0.7	18 arcsec × 18 arcsec 0°	This work
C494α	LOFAR LBA	2	65 arcsec × 45 arcsec 100°	Oonk et al. (2017)
C539α	LOFAR LBA	2	65 arcsec × 45 arcsec 100°	Oonk et al. (2017)
HI–21 cm	VLA	0.65	7 arcsec × 7 arcsec 0°	Bieging et al. (1991)
1667 MHz–OH	VLA	1.3	7 arcsec × 7 arcsec 0°	Bieging & Crutcher (1986)
^{13}CO(1–0)[b]	NRAO 12 m	0.13	56 arcsec × 56 arcsec 0°	Liszt & Lucas (1999)
CO(2–1)[c]	SMT	0.3	33 arcsec × 33 arcsec 0°	Kilpatrick et al. (2014)
[C I] $^3P_1$–$^3P_0$	KOSMA	0.63	54 arcsec × 54 arcsec 0°	Mookerjea et al. (2006)
[C II]	Herschel PACS[d]	250	12 arcsec × 12 arcsec 0°	Salas et al. (2017)
A_V			35 arcsec × 35 arcsec 0°	De Looze et al. (2017)

[a]Observing beam major axis, minor axis and position angle. [b]^{12}CO(2–1) is also available from the same observations.
[c]^{12}CO and ^{13}CO.
[d]Herschel is an ESA space observatory with science instruments provided by European-led Principal Investigator consortia and with important participation from NASA.

details about the observations collected from the literature we refer the reader to the original works (Table 1).

2.1 Wsrt data

The WSRT data used in this work is the same presented in Oonk et al. (2017). The data reduction steps are the same up to the imaging part. Before imaging, we subtracted the continuum from the calibrated visibilities using *CASA*'s (McMullin et al. 2007) *uvcontsub* (see e.g. van Gorkom & Ekers 1989; van Langevelde & Cotton 1990). We use a first order polynomial which is fit to line free channels at both sides of the α lines when possible. After this we imaged the continuum subtracted data using Briggs weighting (Briggs 1995). We tested using different robust parameters to determine the best trade-off between sensitivity and resolution. Using a robust factor of -1 provided the best angular resolution $\theta \leq 70''$ for most subbands (40 out of the 6×8 subbands). A robust factor of 1 provides a factor of two lower spectral noise with a synthesized beam size of $\theta \leq 100''$ (47/48 subbands). We use the cubes generated with a robust of -1 since we are interested in the spatial structure of the line. After imaging we stack the cubes and apply a bandpass correction in the image plane. The stacked cube has a spatial resolution of $70''$ and contains 40 α RRL transitions.[1] The stacked line profile corresponds to RRLs with an average n of 268. After this we compared the stacked line profile extracted from over the face of Cas A with those presented by Oonk et al. (2017). This comparison showed that the spectra agree within errors.

To study the distribution of the weaker C268α -38 km s^{-1} velocity components, we convolve the spectral axis of the cube to increase the signal-to-noise ratio. As convolution kernel we use a boxcar four channels wide. This also produces a cube with a similar velocity resolution as that of the C539α cube (see Table 1). In order to allow for a better comparison between the C268α and C539α lines, we regrid the spectral axis of the C268α cube to match that of the C539α cube.

Of the CRRL data used in this work, the one coming from the WSRT observations is the one with the coarsest spatial resolution.

[1] A line involving a change in principal quantum number of $\Delta n = 1$ is called an α line.

2.2 LOFAR HBA data

Cas A was observed with the LOFAR HBA on 2015 December 13 for 4 h (obsid: L415239). This data were taken as part of the LOFAR Cassiopeia A spectral survey (LCASS; PI: J. B. R. Oonk). During the observation, all 23 + 14 Dutch stations were used. These observations cover the 132.6–152.3 MHz range with 195.3125 kHz wide spectral windows. The correlator was set-up to deliver spectral windows with 512 spectral channels. This results in a channel width of 0.75–0.87 km s^{-1}.

Cygnus A was used as amplitude calibrator at the beginning of the observations (obsid: L415237). Phase and amplitude solutions were derived against Cygnus A and then applied to the Cas A data. After transferring the amplitude and phase from Cygnus A, we self-calibrated the Cas A data. We started the self-calibration cycle using a small number of clean iterations and short baselines, then in each repetition of the cycle, a larger number of clean iterations, as well as longer baselines, were used. The cut-off in the baseline length started at 2000 lambdas and increased to 12 000 lambdas. LOFAR has baselines longer than 12 000 lambdas, but we decided to stop at this cut-off because the signal-to-noise ratio drops for higher resolution. After imaging, the cubes were convolved to a common resolution of 18 arcsec. The cubes were then converted to optical depth using $\tau_\nu = I_\nu / I_\nu^{\rm cont} - 1$, where I_ν is the spectrum extracted from the data cubes and $I_\nu^{\rm cont}$ is the continuum determined from a linear fit to line free channels (e.g. Oonk et al. 2014; Salas et al. 2017). Any residual bandpass in the optical depth cubes was corrected in the image plane using an order two polynomial.

After this, the RRL optical depth cubes were stacked. In the frequency range between 132.6 and 152.3 MHz, there are 16α RRLs. From these, we selected four lines that were in spectral windows with low-radio frequency interference during the observations. The stacked cube has α RRLs with an averaged principal quantum number $n = 357$.

2.3 LOFAR LBA data

The data reduction of the LOFAR LBA data is described in Oonk et al. (2017, obsid 40787). For this work, we have split the ∼75 CRRLs present in the 33–57 MHz range into two groups; one group uses the first six CRRLs, which have principal quantum numbers n = 491, 492, 493, 495, 496, 497, and another group with the

remaining CRRLs (see table 2 of Oonk et al. 2017, for the complete list). This division is made in order to study the CRRL profile at a lower n number, where the effects of pressure and radiation broadening are less severe and it is easier to differentiate velocity components (e.g. Oonk et al. 2017). The stacked cubes have α RRLs with averaged principal quantum numbers of 494 and 539.

2.4 Literature data

We complement the spatially resolved LOFAR and WSRT cubes presented in this work with observations from the literature. A summary of the literature observations is presented in Table 1. From the literature, we have selected the following maps: H I–21 cm (Bieging et al. 1991), the 1667 MHz line of OH (Bieging & Crutcher 1986), ^{12}CO(2–1), and ^{13}CO(2–1) (Kilpatrick et al. 2014), 492 GHz [C I] Mookerjea et al. (2006), and 158 μm [C II] (Salas et al. 2017). Additionally, we include the dust-derived interstellar extinction A_V map of De Looze et al. (2017).

To compare observations with different angular resolutions, we convolve the maps to a common resolution of 70 arcsec. We use 70 arcsec to match the resolution of the WSRT cubes. Two exceptions are the 158 μm [C II] cube and A_V map. We do not convolve the 158 μm [C II] cube since the area covered by each PACS observation is smaller (45 arcsec × 45 arcsec) than the target resolution. As for the dust-derived A_V map, we do not convolve because the images used to model the dust emission were analysed at 35 arcsec resolution (De Looze et al. 2017).

3 RESULTS

3.1 Global velocity structure

In terms of the line-of-sight structure, the gas towards Cas A is observed in various ISM tracers in at least four velocity components. One component corresponds to gas in the local Orion spur at velocities close to 0 km s^{-1} (all velocities are referenced with respect to the local standard of rest). The remaining velocity components, and main focus of this work, are associated with the Perseus arm of the Galaxy at velocities of −47, −41, and −36 km s^{-1}. These last two velocity components have been treated as a single velocity component at −38 km s^{-1} in previous CRRL studies, because they are difficult to separate (e.g. Payne et al. 1994; Kantharia et al. 1998; Oonk et al. 2017). Here, we use this nomenclature when we are not able to separate the −41 and −36 km s^{-1} velocity components.

To compare the line profiles, we averaged the pixels covering the face of Cas A. We define the face of Cas A as a circle of radius 2.5 arcmin centred on $(\alpha, \delta)_{J2000} = (23^h23^m24^s, +58°48'54'')$. The spectra are shown in Fig. 2. In this figure, we highlight the position of three velocity components at −47, −41, and −36.5 km s^{-1}. When the spectra shows the presence of these three velocity components, we notice that the velocity of the line peak agrees between different tracers. For the −38 km s^{-1} velocity component, we can see that the line profile is a blend of two or more velocity components. This is more readily seen in the line profiles of C268α, ^{12}CO, and 1667 MHz OH, where two velocity components are observed, one close to −41 km s^{-1} and other at −36.5 km s^{-1}.

3.2 Channel maps

Here, we present spatially resolved C268α and C539α optical depth cubes. The C357α and C494α maps will be shown later (in Section 3.3), as these show a spatial distribution very similar to that of the C268α and C539α lines (Figs 3 and 4).

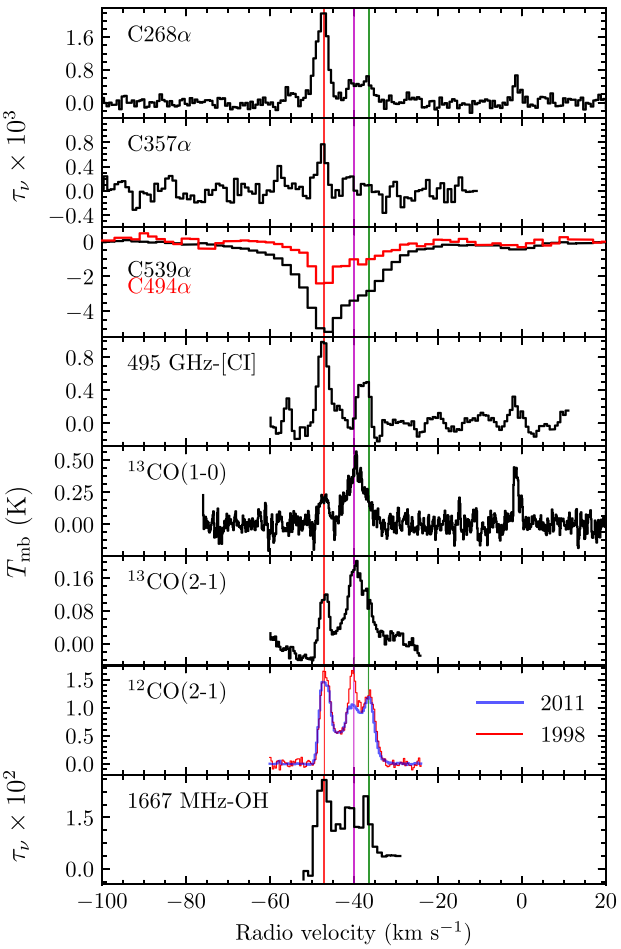

Figure 2. Comparison between the spectra of C268α, C357α, C539α, 492 GHz [C I], ^{13}CO(1–0), ^{13}CO(2–1), ^{12}CO(2–1), and 1667 MHz OH. The three CRRLs and the OH line are shown in optical depth units, while the [C I] and CO lines in brightness temperature units. The spectra where extracted from an aperture defined by the extent of the 1667 MHz OH line map. The Perseus arm velocity components at −47, −41, and −36.5 km s^{-1} are shown with *red*, *magenta,* and *green* lines, respectively. The difference in the 1998 and 2011 ^{12}CO(2–1) line profiles is due to the different choice of off-source position.

C268α channel maps at velocities around that of the −47 km s^{-1} velocity component are shown in Fig. 3. These maps show that the gas is predominantly concentrated to the southwest of Cas A. At around −47 km s^{-1}, there is emission in an elongated structure running from Cas A's western hot spot to its south. This has been labelled with a white line between the W and S (Fig. 3). Higher resolution OH observations show that there are three OH clumps over this W-S structure at a velocity ∼−47 km s^{-1} (clumps B, D, and E; Bieging & Crutcher 1986). However, since OH and CRRLs do not trace exactly the same gas, we cannot use this as evidence that the W-S structure is a collection of clumps. With the resolution of the cubes presented in this work, it is not possible to distinguish if this is a filament or unresolved clumps.

Channel maps showing velocities corresponding to the Perseus arm features of the C268α and C539α lines are presented in Fig. 4. Here, we use the velocity averaged C268α cube to emphasize features close to −38 km s^{-1}. Emission from the C268α −38 km s^{-1}

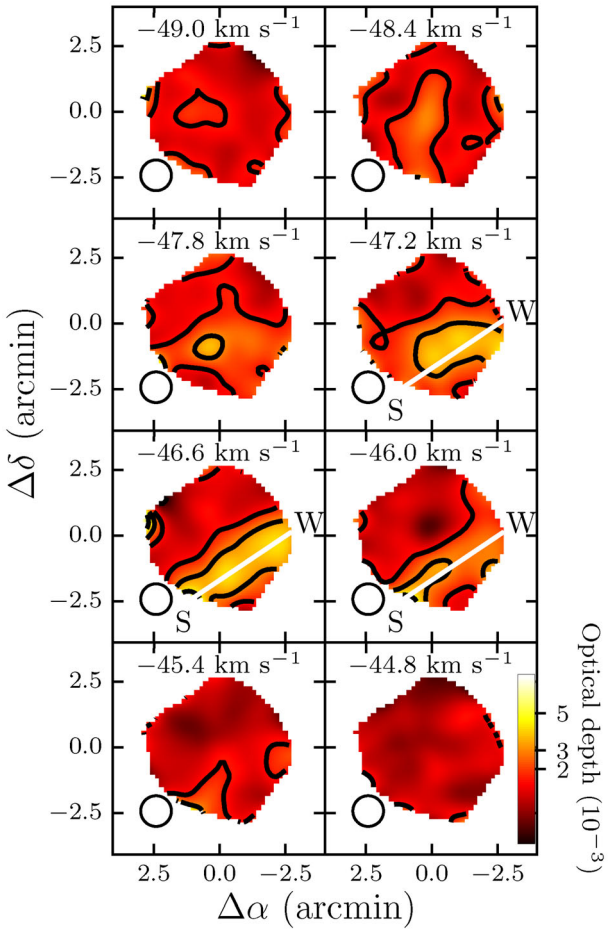

Figure 3. C268α emission around $-47\,\mathrm{km\,s^{-1}}$ channel maps. These maps have a spatial resolution of 70 arcsec, shown in the lower left corner of each panel. The contours start at 3σ, with $\sigma = 6 \times 10^{-4}$, and continue at values of 4σ, 5σ, and 6σ. The white line marks the location of an elongated structure with a W-S orientation.

velocity component is located in the western side of Cas A as well as in the northeast, with a clump close to the centre of Cas A between -43 and $-41\,\mathrm{km\,s^{-1}}$. This central clump is also identified in OH and CO (Bieging & Crutcher 1986; Wilson et al. 1993).

In the C539α maps, we can see similar structures to those seen in the C268α maps, albeit with more detail due to the higher signal-to-noise ratio of the LOFAR data. The W-S structure is visible between -49 and $-37\,\mathrm{km\,s^{-1}}$. The larger extent in velocity is partially due to (radiation or pressure) broadening of the lines at high n (e.g. Salgado et al. 2017b). The spatial distribution of the C539α $-38\,\mathrm{km\,s^{-1}}$ velocity component is harder to interpret due to the blending of the Perseus arm velocity components. If we assume that absorption at the more positive velocities is mainly due to the $-38\,\mathrm{km\,s^{-1}}$ velocity component, then the absorption close to $-33\,\mathrm{km\,s^{-1}}$ should be representative. At this velocity, we see that the absorption comes primarily from the east and west of Cas A, like the C268α emission from this velocity component.

3.3 CRRL properties

The properties of low-frequency CRRLs can be used to determine the gas electron density, temperature, and pressure. These properties imprint their signature in the line integrated optical depth as a function of principal quantum number n (e.g. Shaver 1975; Salgado et al. 2017a). Additionally, the change in line width with n, caused by radiation and pressure broadening, also provides information about the gas properties (e.g. Shaver 1975; Salgado et al. 2017a).

To determine the line properties over the face of Cas A on a pixel-by-pixel basis, we fit the line profiles and construct moment maps. In order to fit the line profiles we first determine where the lines are detected by using the moment masking method as refined by Dame (2011). In this method, the data cube is smoothed to a resolution that is two times the original cube resolution in the spatial and spectral directions. Using the smoothed cube, we search for significant detections by requiring that the signal-to-noise ratio is above some threshold level. For each pixel/channel that shows a significant detection we also set the neighbouring pixels that are inside the convolution kernel as detections. Then we fit the line profile only in those regions where there are significant detections.

To determine an optimum threshold level, we tested using synthetic data cubes. In this test, we varied the threshold level between one and ten times the noise in the synthetic data cube and compared the recovered moment 0 with the known input. This test shows that if we use a threshold of three times the noise in the smoothed cube, then the line properties can be recovered with no significant deviation from the input data. For these observations, this means that for the higher signal-to-noise line at $-47\,\mathrm{km\,s^{-1}}$, we should recover most of the line structure. However, for the weaker velocity component at $-38\,\mathrm{km\,s^{-1}}$, we are likely to recover only the brightest regions.

To fit the RRLs with principal quantum number 268, we use Gaussian line profiles. We fit up to three CRRLs close to -47, -38, and $0\,\mathrm{km\,s^{-1}}$. Once we have the line properties from the $n = 268$ CRRLs, we use their second and third moments to guide the fit for the higher n lines. In the case of the $n = 357$ lines, this is necessary given the lower signal-to-noise ratio. For the $n = 494$ and 539 lines, this is done to guide the separation of the blended line profiles. This relies on the assumption that the CRRLs at different frequencies will trace gas with similar properties. Studies that cover a larger frequency range than the one studied here show that the line properties can be accurately modelled by a single set of gas properties (Oonk et al. 2017). With this the line centroid should be the same for different n lines, and for $n \leq 500$ the line profile is dominated by the gas thermal motion (Salas et al. 2017), which does not depend on frequency.

To fit the C357α lines, we use two Gaussian profiles, one for the $-47\,\mathrm{km\,s^{-1}}$ velocity component and one for $-38\,\mathrm{km\,s^{-1}}$. When fitting, we fix the line centroid and line width to those of the C268α line. This leaves the line amplitude as the only free parameter.

To fit the C494α and C539α lines, we use two Voigt profiles, one for the $-47\,\mathrm{km\,s^{-1}}$ velocity component and one for $-38\,\mathrm{km\,s^{-1}}$. When fitting, we fix the line centroid and the Doppler core of the line profiles to those of the C268α lines. This leaves the amplitude and Lorentz width as free parameters. When there is no significant C268α line emission we adopt the median values from the C268α moments as initial guesses for the line parameters, but we allow them to vary. This is mostly the case for the line at $-38\,\mathrm{km\,s^{-1}}$.

The moment maps for the $n = 268$ RRL at $-47\,\mathrm{km\,s^{-1}}$ are shown in the top row of Fig. 5. Here, we see that emission from the $-47\,\mathrm{km\,s^{-1}}$ velocity component extends almost all over the face of Cas A, with a lower integrated optical depth to the north of the remnant. The moment 0, or velocity integrated optical depth, map for the $-47\,\mathrm{km\,s^{-1}}$ velocity component shows that most of the emission comes from the W-S structure. The moment 1, or optical depth weighted velocity centroid, map shows that over the

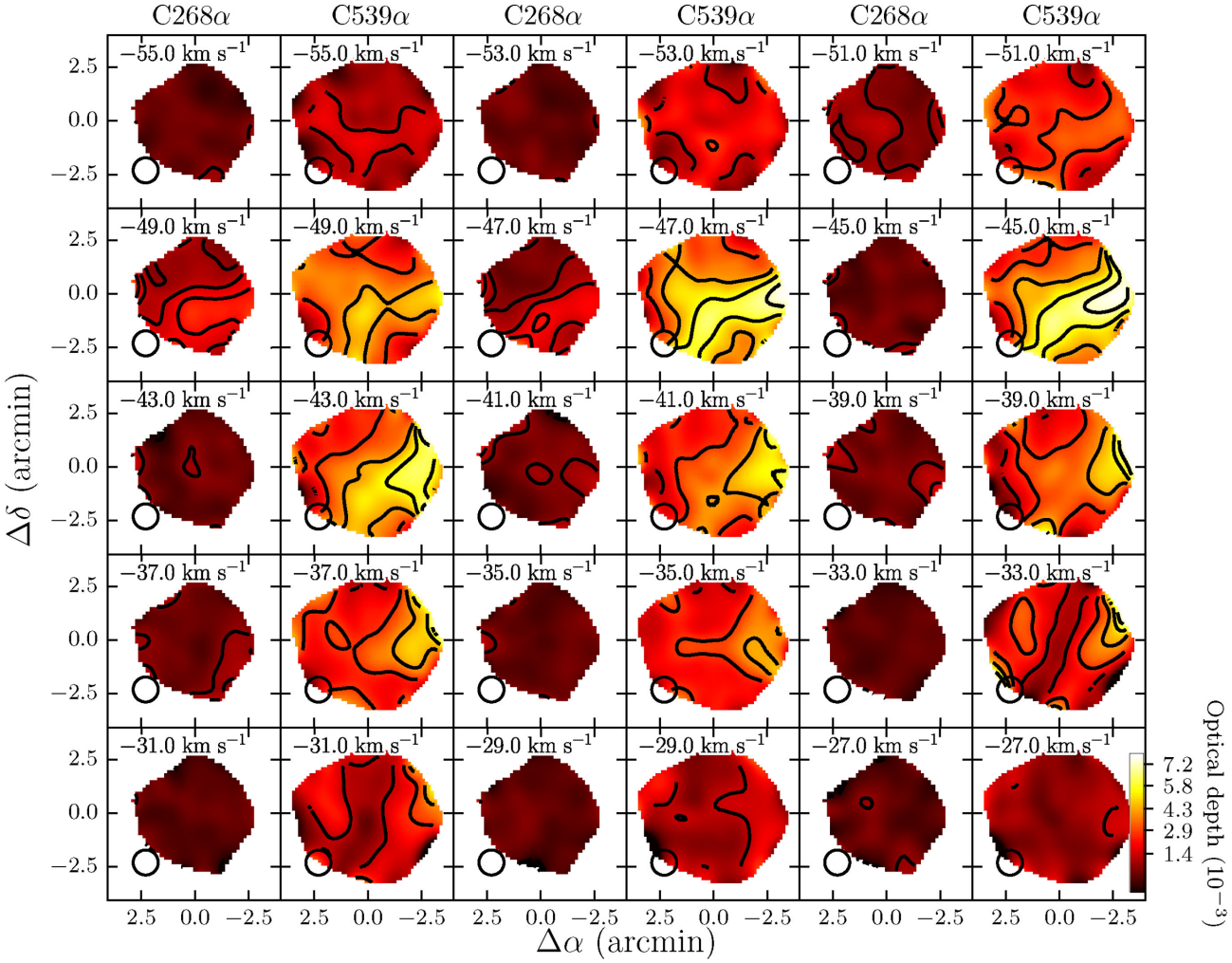

Figure 4. C268α emission and C539α absorption channel maps. The spectral axis of the C268α cube was convolved to a 2.4 km s^{-1} velocity resolution and regrided to match the spectral axis of the C539α cube. The colour scale is the same for both C268α emission and C539α absorption. The contours start at 3σ with $\sigma = 2.5 \times 10^{-4}$ for C268α and $\sigma = 4.8 \times 10^{-4}$ for C539α. The 70″ resolution of the channel maps is shown in the bottom left corner of each map.

W-S structure the velocity remains constant. The moment 2, or full width at half-maximum, map shows that the line is narrow in the West and broadens to the East of Cas A. Towards the north-east of Cas A the −47 km s^{-1} C268α line is broader by a factor of ∼2 with respect to the W-S structure. The CRRL at 0 km s^{-1} is not displayed because at 70 arcsec resolution the signal-to-noise ratio is lower than three in individual pixels.

The moment maps for the C357α −47 km s^{-1} velocity component are shown in the middle panels of Fig. 5. These show that the velocity integrated optical depth of the −47 km s^{-1} velocity component is larger in the W-S structure, similar to that observed in the C268α line.

The moment maps for the C539α line at −47 km s^{-1} are shown in the bottom panels of Fig. 5. These show that most of the C539α absorption from the −47 km s^{-1} velocity component comes from the W-S structure, in accordance with the lower n lines. The moment 2 maps suggests that the −47 km s^{-1} velocity component is broader towards the south-east of Cas A; however, the line width is consistent with a constant value over the face of Cas A.

The moment maps for the C268α and C539α −38 km s^{-1} velocity component are shown in Fig. 6. The C268α line is only detected towards the western hot spot of Cas A. In contrast, the C539α line is detected almost all over the face of Cas A. Both maps show that the peak integrated optical depth is located towards the western hot spot of Cas A. For the C357α line at −38 km s^{-1}, the spatial distribution is similar to that of the C268α at the same velocity, a patch ∼0.4 arcmin towards the south of the western hot spot of Cas A.

The moment 2 maps for the −38 km s^{-1} component shows that the line is broader towards the northern half of Cas A, with the broadest line towards the east. The minimum line broadening is observed towards the centre and south of Cas A. This resembles the ridge of CRRL absorption that passes through the centre of Cas A between −33 and −31 km s^{-1} (Fig. 4).

3.4 Physical conditions from CRRLs

The change in the CRRL profile as a function of principal quantum number has the signature of the gas physical conditions imprinted on it (Shaver 1975; Salgado et al. 2017a). The gas properties that can be determined using CRRLs are its electron density n_e, electron temperature T_e, and the intensity at 100 MHz of the radiation field the carbon atoms are immersed in, $T_{r,100}$.

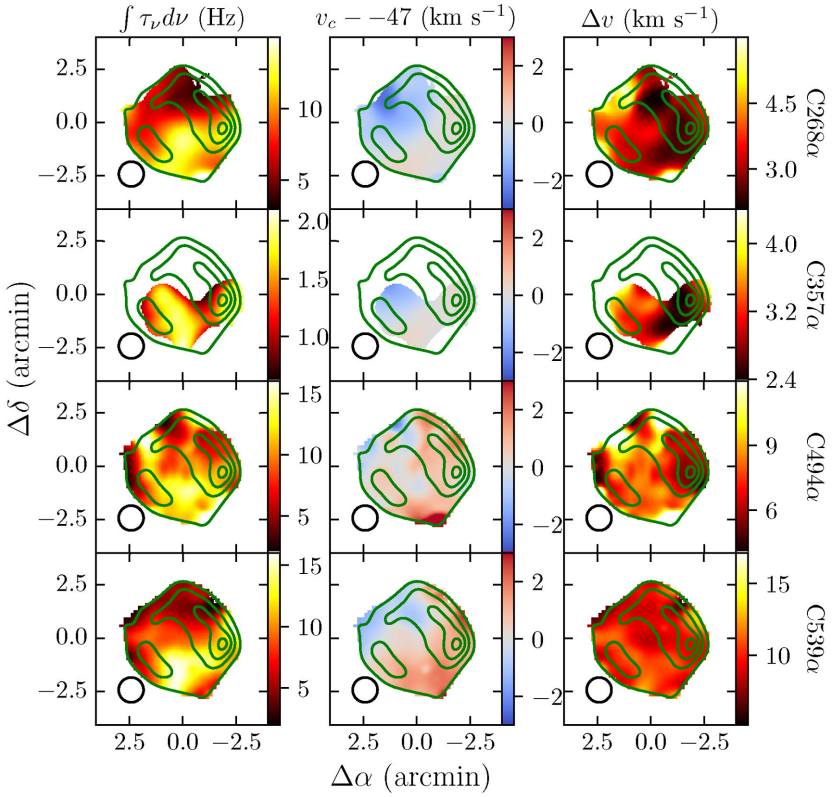

Figure 5. Moment maps for the CRRLs at $-47\,\mathrm{km\,s^{-1}}$. The *top row* shows the moment maps for the C268α line, the *upper middle row* for the C357α line, the *lower middle row* for the C494α line, and the *bottom row* for the C539α line. The *left column* shows the integrated optical depth, the *middle column* the velocity centroid of the line with respect to $-47\,\mathrm{km\,s^{-1}}$ and the *right column* the full width at half-maximum of the line. The *green contours* show the 345 MHz continuum from Cas A at 51 arcsec × 45 arcsec resolution. The 70 arcsec resolution of the moment maps is shown in the bottom left corner of each map. At the edges of Cas A, the signal-to-noise ratios are lower due to the fainter continuum.

To determine the CRRL properties, we use the models of Salgado et al. (2017a). To solve the level population problem, we assume that collisions with atomic hydrogen and electrons set the relative population of carbon ions in the $^2P_{1/2}$ and $^2P_{3/2}$ states. For the collisional rates, we adopt the values of Tielens & Hollenbach (1985) for collisions with hydrogen and those of Hayes & Nussbaumer (1984) for collisions with electrons. We adopt electron and carbon abundances of 3×10^{-4}, while solving the level population problem. However, when converting to per hydrogen atom quantities, we adopt electron and carbon abundances of 1.5×10^{-4}. The effect of these assumptions is small (∼10 per cent) and will be discussed later. For the ℓ-changing collisional rates, we use the semiclassical formulation of Vrinceanu, Onofrio & Sadeghpour (2012) incorporated into the Salgado et al. (2017a) models. Additionally, when solving the level population problem, a radiation field with a power-law shape is included. This radiation field has a spectral index of −2.6, similar to the observed spectral index of Galactic synchrotron emission (e.g. de Oliveira-Costa et al. 2008; Zheng et al. 2017), and its intensity is defined at 100 MHz by $T_{r,100}$ (Shaver 1975; Salgado et al. 2017a).

In order to model the gas properties, we assume that the radiation field the gas is immersed in is constant. Since we are studying gas on scales of $\lesssim$1 pc and the gas is at a distance of $\gtrsim$220 pc from Cas A (e.g. Kantharia et al. 1998; Salas et al. 2017), the possible contribution of Cas A to the radiation field (Stepkin et al. 2007) will change by a negligible amount over the observed structure. Additionally, there are no other known strong, low-frequency, discrete radiation sources in the field. Considering this, it seems reasonable to assume that the gas is immersed in a constant radiation field. Following the results of Oonk et al. (2017), we adopt $T_{r,100} = 1400$ K.

Given the C268α, C357α, C494α, and C539α velocity integrated optical depths, we explore how these can be used to constrain the gas properties. We do not attempt to model the change in integrated optical depth as a function of n, like Oonk et al. (2017) did, given that the number of free parameters is similar to the number of data points. Instead, we use the ratios between these lines. We will use the notation $R^n_{n'}$ to denominate the C$n\alpha$/C$n'\alpha$ line ratio, e.g. C357α/C539α line ratio will be R^{357}_{539}.

To generate R^{268}_{539}, R^{268}_{494}, and R^{357}_{539} from the observations, we use the respective velocity integrated optical depth maps (Figs 5 and 6). These line ratios are shown in Fig. 7. In the case that one of the lines is not detected in one of the pixels we adopt the 3σ upper/lower limit on the integrated optical depth for the non-detection. If two lines are not detected on a pixel we do not attempt to constrain the gas physical conditions. This limits our analysis for the $-38\,\mathrm{km\,s^{-1}}$ velocity component to the western hot spot of Cas A, where the C268α line is detected (Fig. 6).

The line ratios as a function of gas properties in the n_e–T_e plane are shown in Fig. 8 for three different locations in the map (see Figs 7 and 9). As a result of the C268α line being in emission and the C539α line in absorption R^{268}_{539} produces contours that have a similar shape to the constraint imposed by the transition from emission to absorption (Salgado et al. 2017b). The situation is similar for R^{268}_{494}. However, intersecting the R^{357}_{539} constraint with either R^{268}_{539} or R^{268}_{494}

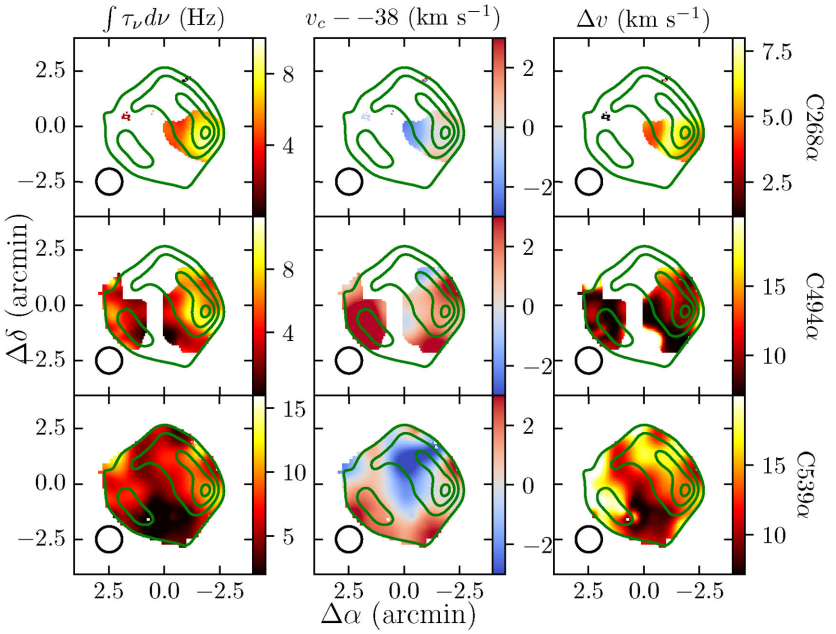

Figure 6. Moment maps for the CRRLs at $-38\,\mathrm{km\,s^{-1}}$. The *top row* shows the moment maps for the C268α line, the *middle row* for the C494α line and the *bottom row* for the C539α line. The *left column* shows the integrated optical depth, the *middle column* the velocity centroid of the line with respect to $-38\,\mathrm{km\,s^{-1}}$ and the *right column* the full width at half-maximum of the line. Here, we do not show the C357α line moments as they are similar to those of the C268α line. The *green contours* show the 345 MHz continuum from Cas A at 51 arcsec × 45 arcsec resolution. The 70 arcsec resolution of the moment maps is shown in the bottom left corner of each map. At the edges of Cas A, the signal-to-noise ratios are lower due to the fainter continuum.

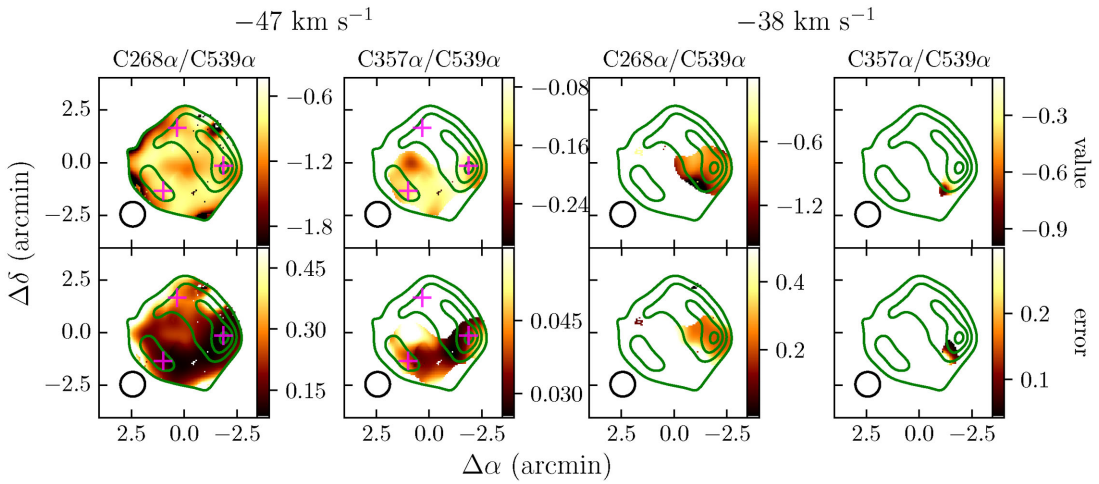

Figure 7. Ratios between different CRRLs at different velocities. The ratios shown are the R_{539}^{268} =C268α/C539α and R_{539}^{357} =C357α/C539α line ratios. The *top panels* show the ratio value and the *bottom panels* the error on the ratio. The *text on top of each column* indicates which ratio is shown in the corresponding column, and a *text label* on the top of the figure shows the velocity component. The ratios show only regions where both lines involved have been detected with a signal-to-noise ratio larger than three. The *pink crosses* in the top panel show the regions used in Fig. 8. The 70 arcsec resolution of these maps is shown in the bottom left corner of each map.

restricts the range of allowed n_e and T_e values. The left-hand panel of Fig. 8 shows that the CRRL ratios used can constrain the gas properties in regions with high signal-to-noise ratio detections. Yet it also reveals that when one of the lines is not detected it is not possible to constrain the gas properties (e.g. right-hand panel in Fig. 8). In this case, the line ratios constrain the gas electron density and place a lower limit on the gas temperature. An upper limit on the gas temperature can be obtained if we consider the implied gas path length. If we restrict the models to path lengths smaller than 200 pc, this effectively puts an upper limit on the electron temperature of ≈160 K (Fig. 8). We adopt an upper limit of 200 pc since we do not expect the gas structures to be larger than this in the line-of-sight direction.

Maps with the electron density, temperature, and pressure constraints derived from the line ratio analysis for the $-47\,\mathrm{km\,s^{-1}}$ velocity component are shown in Fig. 9. The electron density shows almost no variation over the face of Cas A, while the electron temperature and pressure show a slight decrease towards the south. The

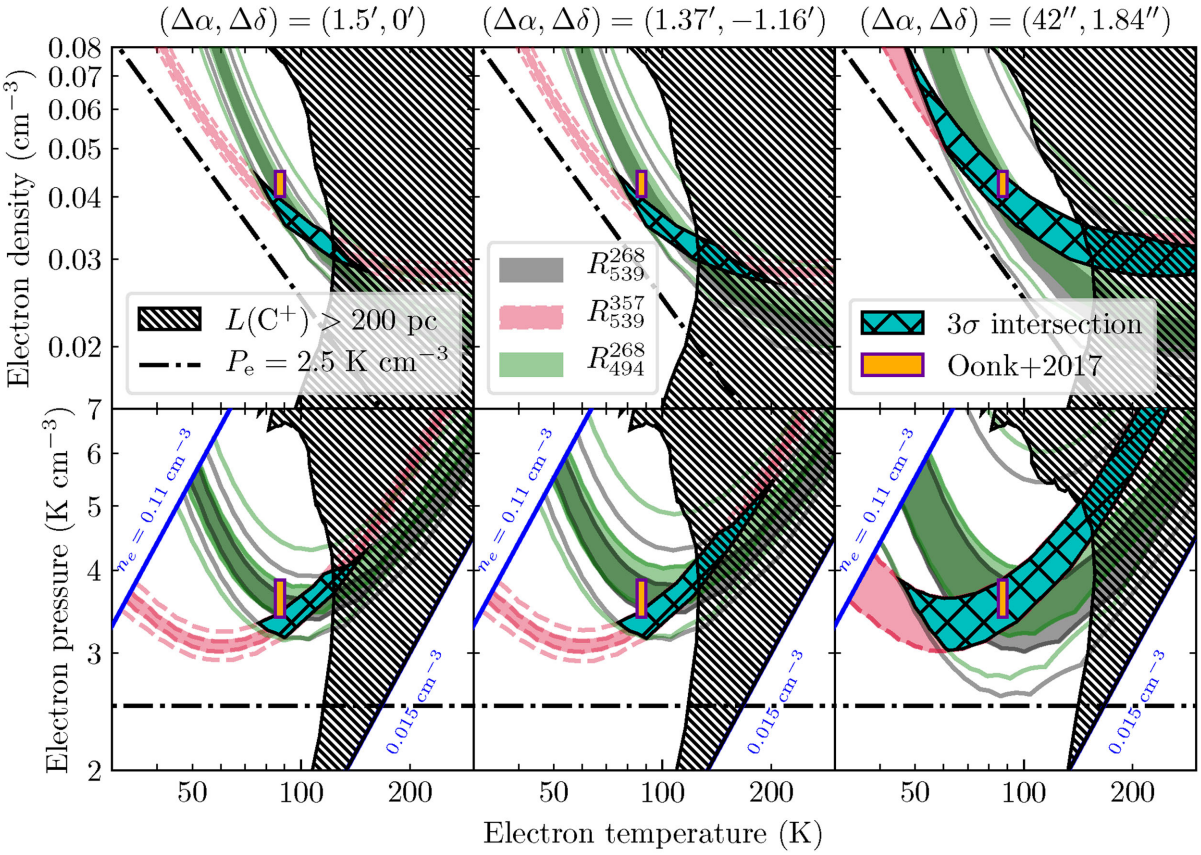

Figure 8. Constraints imposed by the R^{268}_{539} =C268α/C539α, R^{357}_{539} =C357α/C539α, and R^{268}_{494} =C268α/C494α line ratios in the n_e–T_e plane (*top panels*) and in the P_e–T_e plane (*bottom panels*). The constraints are shown for the -47 km s^{-1} velocity component at three different positions in the map. The positions, relative to the map centre, are shown on the top of the corresponding column. These positions are shown in Figs 7 and 9 as green crosses. The *orange rectangle with purple borders* shows the gas physical conditions derived by Oonk et al. (2017). The *dot–dashed line* shows a curve of constant electronic pressure. The *cyan region hatched with black lines* shows the intersection of the constraints imposed by the R^{268}_{539}, R^{357}_{539}, and R^{268}_{494} line ratios if we consider their 3σ ranges. The *densely hatched region* shows where the required ionized carbon path length is larger than 200 pc. *Blue lines* in the bottom row show the limits of the grid of CRRL models.

electron density has an almost constant value over the face of Cas A; however, this largely due to the resolution of the model grid. In the density axis, we have 18 resolution elements, while on the temperature axis we have 78 (Table 2). The discrete nature of the grid of models used to determine the electron temperature and density also results in abrupt changes in the gas properties. Additionally, this discreteness can produce patches that have sizes smaller than the spatial resolution of the data. This effect is particularly notorious in the T_e map (Fig. 9).

As it is evident in Fig. 8, we are constraining the gas properties to a given range. The size of this range will depend on the error bars of each pixel. For pixels with high signal-to-noise ratio (left and centre panels in Fig. 8), the uncertainty in electron density is about ∼30 per cent and in electron temperature ∼25 per cent. While on pixels with lower signal-to-noise ratio (right-hand panel in Fig. 8), the uncertainty can be of a factor of 3 or more. A change of about 25 per cent in electron temperature translates into a 65 per cent change in emission measure. In Table 3, we present the gas properties averaged over the face of Cas A. In this table, we provide the parameter ranges if we consider the 1σ uncertainties in the observed line ratios. In terms of the spatial distribution, this shows little change when we consider the uncertainties. The biggest change is on the mean value.

To estimate the hydrogen density from the electron density, we assume that 94 per cent and 100 per cent of free electrons come from carbon for the -47 and -38 km s^{-1} velocity components, respectively (Oonk et al. 2017). Additionally, we adopt a carbon abundance relative to hydrogen of 1.5×10^{-4} (Sofia et al. 1997). With this, the hydrogen density is 210–360 and 200–470 cm^{-3} for the -47 and -38 km s^{-1} velocity components, respectively.

The largest uncertainty in the derived gas properties comes from the separation between the -47 and -38 km s^{-1} velocity components for the $n > 400$ lines. We test this effect by varying the integrated optical depth of the C539α line and comparing the derived values of n_e and T_e. We find that the electron temperature has an almost linear relation with the integrated optical depth of the C539α line, i.e. if we decrease the C539α line integrated optical depth by 30 per cent, then the derived electron temperature decreases by 30 per cent. For the electron density, the change is less pronounced. A change of 30 per cent in the integrated optical depth of the C539α line results in a change of less than 15 per cent in the electron density.

Using the electron density and temperature maps and the C268α integrated optical depth, we compute the ionized carbon emission measure, $EM_{C\,II}$, column density, $N(C\,II)$, and its path length along the line of sight, $L_{C\,II}$. To determine the column density and $L_{C\,II}$,

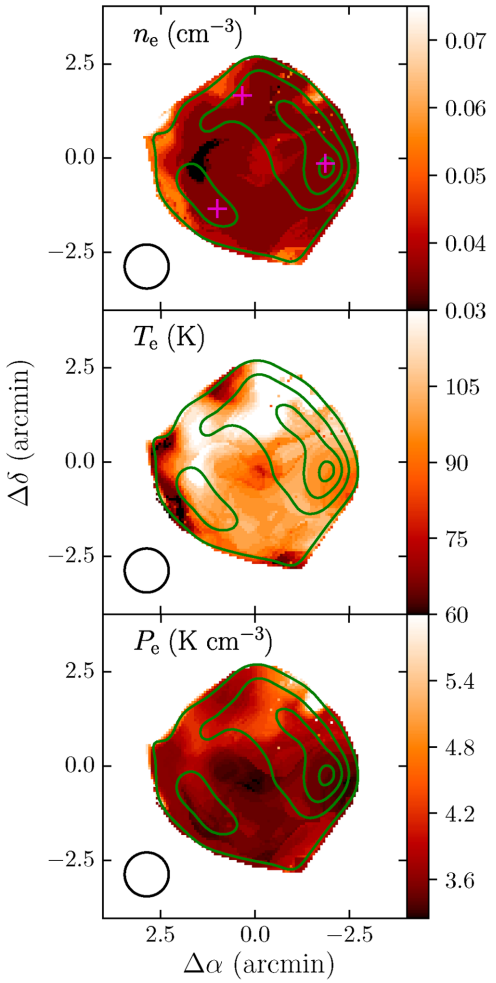

Figure 9. Gas properties derived from the CRRL ratios for the Perseus arm component at $-47\,\mathrm{km\,s^{-1}}$. The *top panel* shows the electron density, the *middle panel shows* the electron temperature, and the *bottom panel* shows the electron pressure. These are derived under the assumption of a constant radiation field of 1400 K at 100 MHz. The *pink crosses* in the top panel show the regions used in Fig. 8. The 70 arcsec resolution of these maps is shown in the bottom left corner of each map.

Table 2. Grid of CRRL models.

Parameter	Notation	Value	Step
Electron density	n_e	0.01–0.1 cm^{-3}	0.005 cm^{-3}
Electron temperature	T_e	10–400 K	5 K
Radiation field	$T_{r,100}$	800–2000 K	400 K
at 100 MHz		and 1400 K	

we assume that 94 per cent of the free electrons come from ionized carbon (Oonk et al. 2017). Maps with EM$_{\mathrm{C\,II}}$, N(C II), and $L_{\mathrm{C\,II}}$ for the $-47\,\mathrm{km\,s^{-1}}$ velocity component are shown in Fig. 10. These show a similar structure to the C268α integrated optical depth map, with larger values towards the south and west of Cas A. The structures smaller than the beam size are due to the strong dependence of the integrated optical depth on the electron temperature ($\propto T_e^{-5/2}$), and the discrete nature of the model grid used. For a constant electron and carbon density, the only variation in the emission measure comes from variations in the path length of the gas along the line of sight. This will also be reflected in the column density $N(\mathrm{C\,II}) = L_{\mathrm{C\,II}} n_{\mathrm{C\,II}}$.

Table 3. Ranges of the mean gas properties over the face of Cas A.

Gas property	Velocity component	
	$-47\,\mathrm{km\,s^{-1}}$	$-38\,\mathrm{km\,s^{-1}}$
T_e (K)	71–137	50–145
n_e (cm^{-3})	0.03–0.055	0.03–0.07
P_e (K cm^{-3})	3.1–4.95	2.7–4.8
$EM_{\mathrm{C\,II}}$ (pc cm^{-6})	0.046–0.26	0.02–0.21
$N_{\mathrm{C\,II}}$ (10^{18} cm^{-2})	3.4–25.9	1.6–18.1
$L_{\mathrm{C\,II}}$ (pc)	27–182	10–180
$n_H{}^a$ (cm^{-3})	210–360	200–470
$N_H{}^a$ (10^{22} cm^{-2})	2.3–17.3	1–12
$A_V{}^b$	11.5–360	200–470

[a]Assuming a carbon abundance relative to hydrogen of 1.5×10^{-4} (Sofia et al. 1997) and that 94 per cent and 100 per cent of the free electrons come from ionized carbon for the -47 and $-38\,\mathrm{km\,s^{-1}}$ velocity components respectively (Oonk et al. 2017).
[b]Adopting $N_H = (2.08 \pm 0.02) \times 10^{21} A_V$ cm^{-2} (Zhu et al. 2017).

We compare the derived gas physical conditions against the spatially unresolved work of Oonk et al. (2017) towards the same background source to check for any differences. We focus on their study as it was the first one which was able to simultaneously explain the line width and integrated optical depth change with n. Additionally, this work and that of Oonk et al. (2017) use the same models, which reduces the need to account for different assumptions in the modelling. If we compare Table 3 with table 7 of Oonk et al. (2017), we see that our results, averaged over the face of Cas A, are consistent.

3.5 158 μm-[C II] line properties

The 158 μm-[C II] line is the main coolant of the neutral diffuse ISM (e.g. Wolfire et al. 1995, 2003). Here, we present the properties of the spatially resolved, velocity unresolved, 158 μm [C II] line.

To determine the properties of the 158 μm-[C II] line, we fit a Gaussian profile to each of the nine PACS footprints. We only fit one Gaussian component since the line is unresolved in velocity. The best-fitting parameters of the Gaussian profile are presented in Table 4. These show little variation in the line frequency integrated intensity, but we do note that the lowest values are found in the northern footprints (5 and 6, see Fig. 11). This could be due to the lower column densities found towards the north of Cas A (see Fig. 10).

If we take the observed luminosity of the 158 μm [C II] line and compare it to the CRRL-derived gas column density, we obtain values of the order of $(1.4 \pm 0.1) \times 10^{-26}$ erg s^{-1} (H-atom)$^{-1}$. This cooling [C II] rate is somewhat less than the cooling rate derived from ultraviolet absorption line studies originating from the upper fine-structure level in sightlines through nearby diffuse clouds ($(3–10) \times 10^{-26}$ erg s^{-1} (H-atom)$^{-1}$; Pottasch, Wesselius & van Duinen 1979; Gry, Lequeux & Boulanger 1992), but comparable to the average cooling rate of the Galaxy [$(2.65 \pm 0.15) \times 10^{-26}$ erg s^{-1} (H-atom)$^{-1}$; Bennett et al. 1994. For the CRRL-derived column densities (Table 3), the 158 μm-[C II] line will be optically thick (e.g. Tielens & Hollenbach 1985). If the [C II] line is optically thick, then the observed line does not account for the total

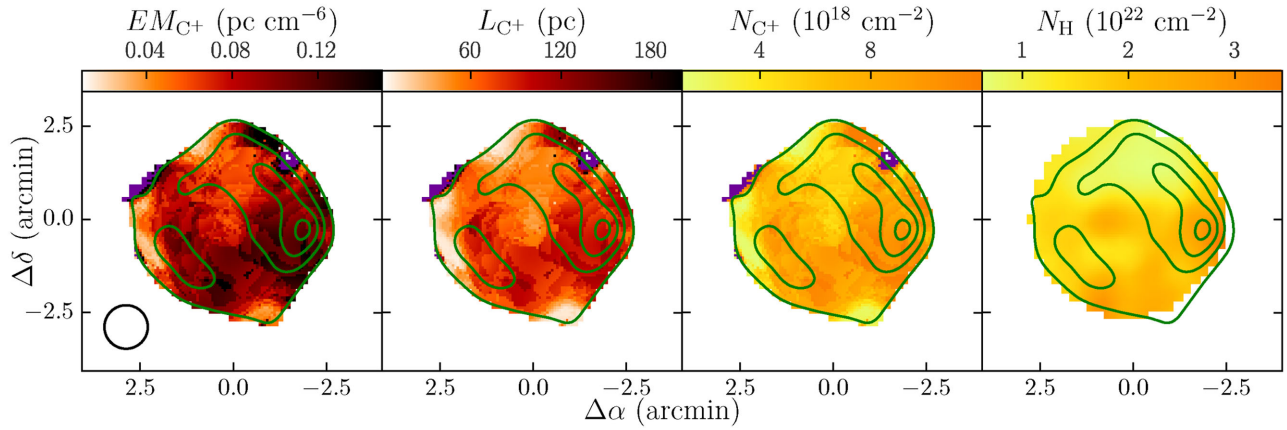

Figure 10. C^+ emission measure $EM_{C\,II}$, path length L_{CII} and column density of ionized carbon $N(C\,II)$ derived from the CRRL analysis for the Perseus arm component at $-47\,km\,s^{-1}$, and the hydrogen column density map derived from the dust analysis by De Looze et al. (2017). The *leftmost column* shows the emission measure, the *middle left column* the path length, the *middle right column* the column density of ionized carbon, and the *rightmost column* the hydrogen column density derived from analysis of the dust emission towards Cas A (De Looze et al. 2017). Regions where we cannot constrain the gas properties given the parameter space explored and observational uncertainties are shown with a colour not present in the colour bar. The 70 arcsec resolution of these maps is shown in the bottom left corner of each map. The *green contours* show the 345 MHz continuum from Cas A at 51 arcsec × 45 arcsec resolution.

Table 4. 158 μm [C II] line properties.

Region	v_c (km s^{-1})	$\int I_\nu d\nu$ (10^{-5} erg cm^{-2} s^{-1} sr^{-1})	$L_{[C\,II]}$ ($L_\odot$)
1	-19 ± 15	6.70 ± 0.11	1.14 ± 0.02
2	-20 ± 15	5.99 ± 0.11	1.02 ± 0.02
3	-18 ± 15	6.15 ± 0.09	1.05 ± 0.01
4	-20 ± 15	6.76 ± 0.12	1.15 ± 0.02
5	-19 ± 15	4.65 ± 0.22	0.79 ± 0.04
6	-23 ± 15	5.10 ± 0.19	0.87 ± 0.03
7	-19 ± 15	6.92 ± 0.08	1.18 ± 0.01
8	-19 ± 15	6.74 ± 0.15	1.15 ± 0.02
9	-15 ± 15	7.14 ± 0.11	1.22 ± 0.02

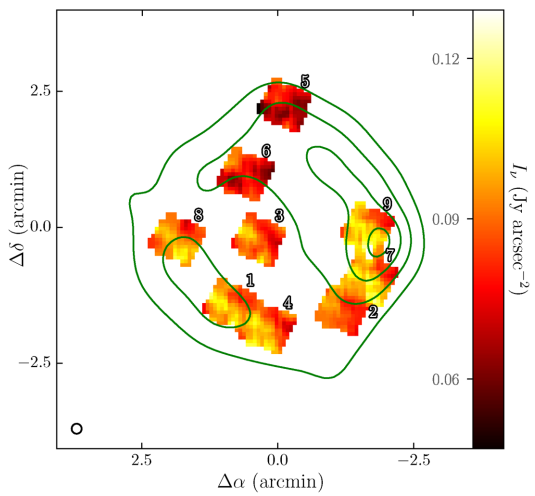

Figure 11. Map of 158 μm [C II] line emission obtained with Herschel PACS. In these, the [C II] line is unresolved in velocity, and only ∼20 per cent of the surface of Cas A is covered. This map is shown at its native resolution of 12 arcsec.

line-of-sight-ionized carbon column that, in turn, results in a lower [C II] cooling rate.

4 DISCUSSION

4.1 Comparison with other tracers

We compare the CRRL optical depth with lines that trace different components of the ISM. These include diffuse atomic gas (21 cm H I; Bieging et al. 1991), diffuse molecular gas (18 cm OH; Bieging & Crutcher 1986), translucent gas (492 GHz–[C I]; Mookerjea et al. 2006), and dense molecular gas (CO; Wilson et al. 1993; Liszt & Lucas 1999; Kilpatrick et al. 2014).

4.1.1 Spatial distribution

A comparison between the optical depths of 21 cm H I, C268α, and the ^{12}CO(2–1) line is presented in Fig. 12. This shows that most of the C268α emission comes from regions where H I is saturated (cyan pixels in the H I maps). The ^{12}CO(2–1) line also shows structures that are well correlated with the ones seen in C268α and 21 cm H I. However, the peaks of CO emission are generally located outside the face of Cas A, which does not allow for a direct comparison. One exception is at a velocity of $-47.8\,km\,s^{-1}$, where a peak of ^{12}CO(2–1) emission is located over the face of Cas A. In this case, the distance between the peaks of ^{12}CO(2–1) and C268α is 87 arcsec.

The spatial distribution of ^{12}CO(2–1) shows that most of the gas at $-41\,km\,s^{-1}$ is located to the west of Cas A, while the gas at $-36.5\,km\,s^{-1}$ extends from the west to the south-east of Cas A (Kilpatrick et al. 2014). Both velocity components overlap towards the west of Cas A. This makes the distinction of these velocity components more difficult in this region.

To explore the relation between CO emission and CRRL emission, we draw a slice joining the peaks of ^{12}CO(2–1) and C268α emission at a velocity of $-47.8\,km\,s^{-1}$. The slice is shown as a green line in Fig. 12 in the panels with a velocity of $-47.8\,km\,s^{-1}$. The normalized intensity or optical depth of different tracers along this slice is shown in Fig. 13. Here, we notice how the optical depth of C268α and Cα(537) peaks at the same location, and the molecular lines peak towards the left of the CRRLs, which corresponds to the south-east direction in the sky. The difference between the peaks of the CRRLs and the molecular lines is similar to that expected

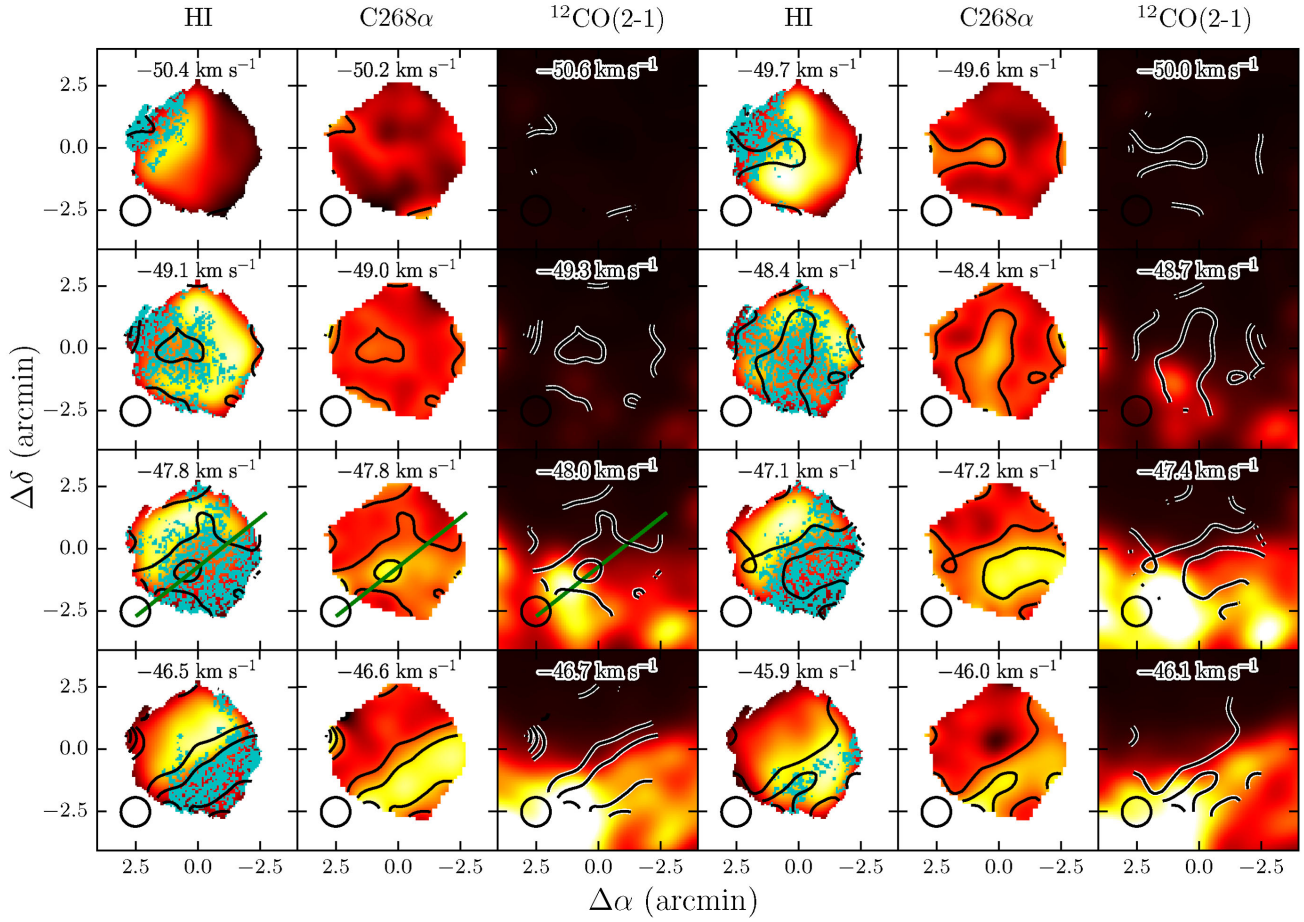

Figure 12. Comparison between the optical depths of 21 cm H I, C268α, and the ^{12}CO(2–1) line brightness. Masked pixels in the 21 cm H I optical depth maps are shown in cyan. The *green line* in the −47.8 km s^{-1} map shows the slice used to study the gas between the peaks of the ^{12}CO(2–1) and C268α lines. The 70 arcsec resolution of these maps is shown in the bottom left corner of each map.

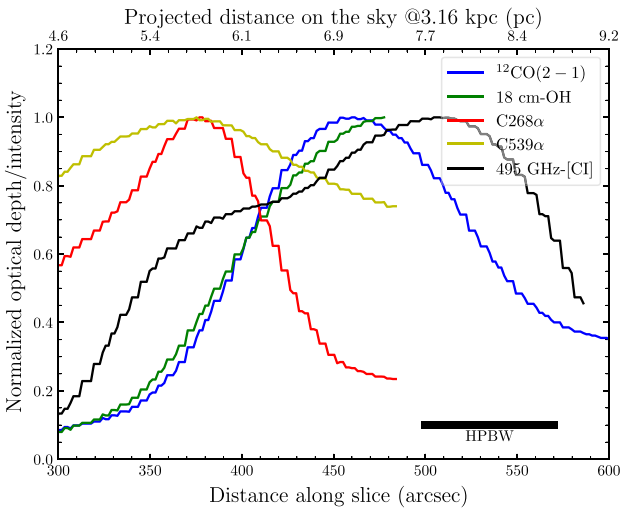

Figure 13. Comparison between different ISM tracers along a slice joining the C268α optical depth peak and ^{12}CO(2–1) line peak at a velocity of −47.8 km s^{-1}. The *black bar* at the bottom shows the half power beam width (70 arcsec) of the images. The *top axis* shows the plane of the sky distance along the slice assuming that the gas is at a distance of 3.16 kpc from the observer (Salas et al. 2017). Given that the gas could be closer to the observer this distance is an upper limit.

in a photodissociation region, (PDR; e.g. Hollenbach & Tielens 1999). As we move towards the south-east of Cas A the gas shows a C II/C I/CO-layered structure, which suggests that we are observing the PDR associated with the edge of a molecular cloud.

The distance at which the gas becomes CO bright will depend on the average PDR density. The projected distance on the plane of the sky between the peak of the C268α optical depth and the peak of the ^{12}CO(2–1) emission is 1.3 ± 0.6 arcmin. If we assume that the Perseus arm gas is at a distance of 3.16 ± 0.02 kpc from Earth in the direction of Cas A (Choi et al. 2014; Salas et al. 2017), then this corresponds to ∼1.2 ± 0.5 pc in the plane of the sky. CO will be sufficiently shielded from photodissociating photons when $A_{\rm FUV} \sim 1$. We adopt a conversion factor between extinction in the V band and hydrogen column density of $N_{\rm H} = (2.08 \pm 0.02) \times 10^{21} A_{\rm V}$ cm^{-2} (Zhu et al. 2017). Then, to convert between optical opacity and far-ultra violet (FUV) opacity, we adopt $\kappa_{\rm d}({\rm FUV}) \approx 1.8\kappa_{\rm d}({\rm V})$. With this, for an $A_{\rm FUV}$ of one magnitude we have $N_{\rm H} = (1.15 \pm 0.01) \times 10^{21}$ cm^{-2}. This implies that the mean density in this PDR is $n_{\rm H} = 310 \pm 28$ cm^{-3}. This density is consistent with the hydrogen density derived from the CRRL analysis (Table 3).

Motivated by the observed layered structure, we compare the CO emission to that of an edge-on PDR model. This model is an extension of the Tielens & Hollenbach (1985) PDR model that includes the updates of Wolfire, Hollenbach & McKee (2010) and

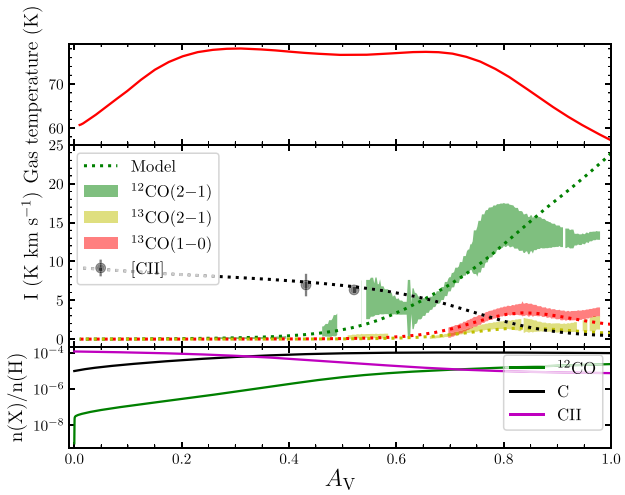

Figure 14. Comparison between the ^{12}CO(2–1), ^{13}CO(1–0), ^{13}CO(2–1), and 158 μm [C II] velocity integrated line intensity along the slice shown in Fig. 13. The observed quantities (*shaded regions*) are compared with a PDR model (*dashed lines*). The *shaded regions* show the observed values and their 3σ error range. The 158 μm [C II] points have been rescaled to be visible in this figure. The PDR model is that of a region with a constant hydrogen density of 300 cm^{-3}, an incident radiation field of $G_0 = 4.2$ on one side of the cloud, and a line of sight optical interstellar extinction of eight. For more details on the PDR model, see the text and Pabst et al. (2017).

Hollenbach et al. (2012). The calculation of line intensities and source parameters for edge-on models are discussed in Pabst et al. (2017). We use a total hydrogen density of 300 cm^{-3}, an A_V of eight along the line of sight and of eight in the transverse direction. The gas in the PDR is illuminated on one side by an interstellar radiation field (ISRF) with $G_0 = 4.2$, measured in Habing (1968) units, and primary cosmic ray ionization rate per hydrogen of 7×10^{-17} s^{-1}. The carbon and hydrogen RRLs observed towards Cas A (Oonk et al. 2017) have been reanalysed by Neufeld et al. (subm) taking into account the relevant chemical recombination routes and we have adopted values of the radiation field and cosmic ray ionization rate consistent with their results. We adopt an abundance ^{12}CO/^{13}CO of 60, appropriate for gas in the Perseus arm in this direction (Langer & Penzias 1990; Milam et al. 2005).

The comparison between observations and the output from the PDR model is presented in Fig. 14. The adopted density ensures that the calculated distance on the sky between the CO peak and the surface of the PDR, as defined by the CRRL peak, agrees with the observations. For $A_V \geq 0.5$, the increase in the line intensity is well described by the model. For $A_V \sim 0.9$, the proximity to the edge of the mapped region causes the velocity integrated line intensity to decrease. This decrease close to the map edge is caused by the convolution with a 70 arcsec beam.

Additionally, we use the same model to predict the velocity integrated line intensity of the 492 GHz [C I] and 158 μm [C II] lines, and the optical depth of the 18 cm OH line. The model does a good job in reproducing the observed optical depth of the OH line. In the region, where the slice intersects footprint 1 of the PACS 158 μm-[C II] cube (Fig. 11), the model predicts a value of 4.3×10^{-5} erg cm^{-2} s^{-1} sr^{-1}. The observed value is 56 per cent larger, which can be accounted for by the presence of gas at higher velocities not present in the model (e.g. the −38 and 0 km s^{-1} velocity components present in the velocity unresolved PACS observations). However, in the case of atomic carbon, the model overestimates the observed values by a factor of 5. This is similar to that found in other lines of sight, where the predicted atomic carbon column density is larger than the observed one (e.g. Gong, Ostriker & Wolfire 2017).

De Looze et al. (2017) find an ISRF with a strength $G_0 \sim 0.6$. This value is lower than the one adopted here, but we do note that against Cas A it is not possible to use the dust spectral energy distribution to estimate the strength of the ISRF. Outside the area covered by Cas A De Looze et al. (2017) find strengths for the ISRF of the order of unity. However, the derived strength of the ISRF will depend on the adopted model with a variation of up to 1.6 depending on the model details (e.g. Fanciullo et al. 2015; Planck Collaboration XXIX 2016). In their work, De Looze et al. (2017) also use line ratios and the PDR toolbox models (Pound & Wolfire 2008) to estimate the strength of the ISRF in the ISM between Cas A and Earth. They find that the line ratios are consistent with their dust-derived value of $G_0 \sim 0.6$, but the line ratio is also consistent with a lower density and stronger ISRF (see figure C1 in De Looze et al. 2017). Based on the current data, we infer that the adopted value is in reasonable agreement with all observations.

4.1.2 *Gas column density*

For the −47 km s^{-1} feature, most of the 21 cm H I optical depth maps show that the line is saturated with values of $\tau \gtrsim 5$ (Bieging et al. 1991). Nonetheless, this lower limit on the optical depth can be used to place a lower limit on the atomic hydrogen column density. If we assume that the width of the 21 cm H I line profile at −47 km s^{-1} is the same as that of the CRRL at the same velocity and that the spin temperature is greater than 50 K, then we have that $N(\mathrm{H\,I}) > 1.5 \times 10^{21}$ cm^{-2}. This limit is consistent with the column density derived from the CRRL and edge-on PDR analysis, and it implies a fraction $N(\mathrm{H\,I})/N(\mathrm{H_2}) \gtrsim 0.1$.

Additional estimates of the gas column density can be obtained from measurements of X-ray absorption and from the dust optical depth. In the case of X-ray absorption, Hwang & Laming (2012) determined values of 2×10^{22} cm^{-2} over the south portion of Cas A, with higher values ($\sim 3 \times 10^{22}$ cm^{-2}) towards its western hot spot. These values are slightly smaller than the ones found using the CRRLs lines. We consider that this difference is not significant, given the uncertainties associated with X-ray column density measurements (e.g. Predehl & Schmitt 1995; Zhu et al. 2017). Recently, De Looze et al. (2017) modelled the dust emission towards Cas A and used it to determine the mass of dust in the ISM along the line of sight. They adopted a dust-to-gas ratio of 0.0056 and found column densities of 1.5×10^{22} cm^{-2} towards the south of Cas A, and 2.2×10^{22} cm^{-2} towards the western hot spot. A map showing the spatial distribution of column density derived from the dust analysis is shown in the rightmost panel of Fig. 10. A comparison between the column densities derived from the dust and CRRL analysis (right-hand panels in Fig. 10) shows good agreement, with larger values towards the South of Cas A and a peak against its western hot spot. To compare their magnitudes, we focus on regions towards the south of the centre of Cas A, where we see less emission from gas at −38 km s^{-1} which would create confusion. Here, the magnitude of the CRRL-derived gas column density, 2.4–11.3 $\times 10^{22}$ cm^{-2}, is comparable to that derived from the dust analysis. The major uncertainty in the determination of the ISM dust content along this line of sight comes from the separation between the foreground ISM dust component and the contribution from dust associated with the supernova remnant. This introduces a factor of a few uncertainty in the derived dust mass and column density.

The CRRL-derived gas column density averaged over the face of Cas A, (3.4–25.9) $\times$ 10^{18} cm^{-2}, on its own implies an hydrogen column density of (2.3–17.3) $\times$ 10^{22} cm^{-2}. Given that not all of the carbon is ionized, we also need to account for carbon in atomic and molecular forms. We focus on a region to the south of the centre of Cas A, following the slice in Fig. 12, where there is CO emission. Here, with an adopted A_V of eight, our PDR model is able to reproduce the CO observations. However, for an A_V of eight and an excitation temperature $\sim$20 K, the CO lines used here are optically thick. This points towards the presence of denser CO-rich clumps embedded in a lower density CO-dark halo. This situation is similar to that observed towards the W43 star-forming region, where large column densities are derived from atomic hydrogen observations at 21 cm ($N_H \approx 2 \times 10^{22}$ cm^{-2}; Bihr et al. 2015; Bialy et al. 2017). Gamma-ray and dust observations in our Galaxy have revealed the presence of large reservoirs of CO-dark molecular gas (with a mass fraction comparable to that of the CO molecular gas; Grenier, Casandjian & Terrier 2005; Planck Collaboration XIX 2011). Likely, much of this gas is in extended atomic hydrogen haloes around giant molecular cloud complexes in spiral arms such as the ones probed in this study in the Perseus arm.

4.2 Envelopes of molecular clouds

The gas properties derived from the CRRL analysis seem to bridge the gap between the atomic gas traced by the 21 cm line of H I and the molecular gas traced by the CO lines in the millimetre (Oonk et al. 2017; Salas et al. 2017). From spatially unresolved observations of the 21 cm H I line in this direction, Davies & Matthews (1972) derived a temperature of 140 $\pm$ 40 K for the two most prominent Perseus arm absorption features at -47 and -38 km s^{-1}. It has not been possible to estimate this value on smaller scales due to the saturation of the 21 cm H I line at these velocities (e.g. Bieging et al. 1991), but it is likely to be slightly colder. On the molecular side of things, we have temperatures of $\sim$20 K (Batrla, Walmsley & Wilson 1984). This would put the gas traced by low-frequency CRRLs, with an electron temperature of $\sim$80 K, in between atomic and molecular gas. A place where this transition takes place is the envelope of molecular clouds (e.g. Moriarty-Schieven & Wannier 1997; Krumholz, McKee & Tumlinson 2009; Sternberg et al. 2014).

Studies of molecular clouds in the solar vicinity show that their atomic envelopes have temperatures of the order $\sim$100 K (Andersson et al. 1991). A comparison between gas traced by the 21 cm H I and the ^{13}CO lines shows that the atomic component is more extended than the molecular one and their velocity fields are not necessarily aligned (Imara & Blitz 2011). The properties of the envelope will depend on the environment. Here, we compare against two giant molecular clouds, both show large fractions of atomic gas, but one shows little star formation, with an infrared luminosity of $\approx$5000 L$_\odot$; G216–2.5 (the Maddalena-Thaddeus cloud; Maddalena & Thaddeus 1985; Williams & Maddalena 1996; Megeath et al. 2009; Imara 2015) and the other a mini-starburst with an infrared luminosity of 3.5 $\times$ 10^6 L$_\odot$ (Motte, Schilke & Lis 2003; Nguyen Luong et al. 2011; Bihr et al. 2015; Bialy et al. 2017). The atomic envelope around G216–2.5 has a thickness of $\sim$50 pc and the atomic gas column density inferred from observations of the 21 cm line of H I is $\approx$2.21 $\times$ 10^{21} cm^{-2} (Williams & Maddalena 1996). Around W43, the atomic envelope has a thickness of 140 pc (Motte et al. 2014), and the atomic gas column density is $\approx$2 $\times$ 10^{22} cm^{-2} (Bihr et al. 2015; Bialy et al. 2017). The later column density is consistent with the lower end of the ranges found here (Table 3).

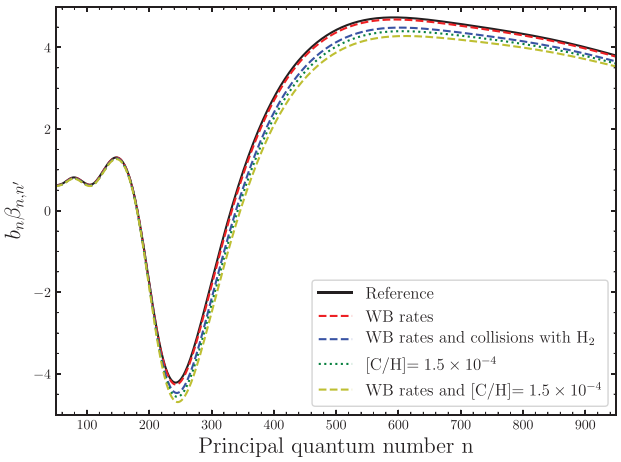

Figure 15. Comparison between CRRL models under different assumptions regarding the carbon ion collisional excitation rates, carbon, and electron abundances. All models were computed for an electron density of 0.05 cm^{-3} and temperature 80 K. The reference model is one computed assuming [C/H] = [e/H] = 3×10^{-4} and using the Tielens & Hollenbach (1985) and Hayes & Nussbaumer (1984) collisional rates. The models labelled with WB rates use the Wilson & Bell (2002) rates for collisions with electrons and those of Barinovs et al. (2005) for collisions with atomic hydrogen. The model that includes collisions with molecular hydrogen, H_2, uses the rate for collisions with molecular hydrogen presented in Goldsmith et al. (2012). The models labelled with [C/H] = 1.5×10^{-4} use this abundance for carbon and electrons. The largest difference for and individual change is produced when the electron and carbon abundances are modified.

Another way in which we can study the envelopes of giant molecular clouds is with observations of the 158 μm [C II] line. In cases where it is possible to isolate an ionized carbon layer around a molecular cloud, it is found that the gas temperature and density are close to those found here. In the Magellanic clouds, Pineda et al. (2017) find densities of 700–2000 cm^{-3} and temperatures of $\sim$50 K.

4.3 Uncertainties in the CRRLmodelling

The change in line properties as a function of physical properties is quite sensitive to the gas physical conditions. During the modelling of the CRRL line properties as a function of principal quantum number a series of assumptions are made which that an effect on the derived gas properties. Some of these have been explored previously, like the use of different angular momentum changing collisional rates (Salgado et al. 2017a), or including collisions with hydrogen when solving the level population problem (Oonk et al. 2017). Additionally, two assumptions have not been explored before; those are the use of different collisional rates for the excitation of ionized carbon and changing the carbon and electron abundances relative to hydrogen. Having different collisional rates and abundances will change the dielectronic capture rate. This will be reflected as a change in the departure coefficient b_n, which determines how the integrated optical depth will behave as a function of n.

Given that it is computationally expensive to recompute the grid of models for each set of assumptions, we focus on a particular point in the n_e–T_e plane. The change in the $b_n\beta_{n,n'}$ coefficients as a function of n is shown in Fig. 15 for different assumptions. These show that the change in the integrated optical depth will be $\sim$10 per cent for the models computed using the different collisional rates and lower carbon and electron abundances. For other assumptions, the difference will be lower.

Recently, Guzmán et al. (2017) and Vrinceanu, Onofrio & Sadeghpour (2017) have investigated the effect of using different formulations (semiclassical versus quantum mechanical) when computing the ℓ-changing collisional rates. As shown by Salgado et al. (2017a, , see their fig. 14), this will affect the departure coefficients, mainly their absolute values. However, as Guzmán et al. (2017) and Vrinceanu et al. (2017) point out, there is no physical reason to prefer one formulation over the other. A more detailed comparison of the effect different formulations will have on the predicted CRRL properties will be investigated in the future.

5 SUMMARY

We have presented 70 arcsec resolution CRRL maps at 340, 148, 54, and 43 MHz. The distribution of the C268α line in emission reveals a good correlation with regions where the 21 cm H I line is saturated and regions of faint ^{12}CO(2–1) emission. We interpret this as as a diffuse PDR, in which low-frequency CRRLs trace the less dense, warmer envelope of molecular gas.

Using the ratios between CRRLs, we have constrained the gas electron temperature and density along the line of sight on scales of $\lesssim$1.2 pc. With the line ratios used here, the constraints result in a range of allowed electron temperatures and densities. Averaged over the face of Cas A, the constraints on the electron density are $n_e = (0.03–0.055)\,\mathrm{cm}^{-3}$ and $T_e = (70–140$ K for gas in the Perseus arm of the Galaxy at $-47\,\mathrm{km\,s}^{-1}$. The pressure shows variations of less than a factor of 2 on $\lesssim$1.2 pc scales.

From the constraints on the electron temperature and density, we derived lower limits for the ionized carbon emission measure, column density and its line-of-sight path length. The lower limit on the column density is $3.4 \times 10^{18}\,\mathrm{cm}^{-2}$, which corresponds to an hydrogen column density of $2.2 \times 10^{22}\,\mathrm{cm}^{-2}$ if all carbon is ionized and $[\mathrm{C/H}] = 1.5 \times 10^{-4}$. The hydrogen density derived from analysis of the CRRLs integrated optical depths is 210–360 cm^{-3}.

A PDR model with an average hydrogen density of 300 cm^{-3}, and conditions similar to those inferred for the clouds in this region, is able to reproduce the observed distribution of ^{12}CO(2–1), ^{13}CO(2–1), ^{13}CO(1–0), and 1667 MHz OH.

The relatively high spatial resolution of the present observations enables us to study the relation between CRRLs and other tracers of the ISM on scales where it is possible to observe the PDR-like structure in the surface of a molecular cloud. This also highlights the importance of CRRLs as tracers of the diffuse ISM, as they allow us to determine the gas physical conditions in regions which are not readily traced by 21 cm H I and/or CO. These observations highlight the utility of CRRLs as tracers of low-density extended H I and CO-dark gas halo's around molecular clouds. Future surveys of CRRLs with the LOFAR are promising, as they could reveal important new clues about the physics of the ISM, particularly about the transition from atomic-to-molecular gas and the properties of CO-dark gas.

ACKNOWLEDGEMENTS

P.S., J.B.R.O., A.G.G.M.T, H.J.A.R. and K.L.E. acknowledge financial support from the Dutch Science Organization (NWO) through TOP grant 614.001.351. LOFAR, designed and constructed by ASTRON, has facilities in several countries, which are owned by various parties (each with their own funding sources), and which are collectively operated by the International LOFAR Telescope (ILT) foundation under a joint scientific policy. We gratefully acknowledge that LCASS is carried out using Directors discretionary time under project DDT001. M.C.T. acknowledges financial support from the NWO through funding of Allegro. M.G.W. was supported in part by NSF grant AST1411827. A.G.G.M.T acknowledges support through the Spinoza premie of the NWO. This research made use of Astropy, a community-developed core PYTHON package for Astronomy (Astropy Collaboration et al. 2013), and of NASA's Astrophysics Data System. The LOFAR software and dedicated reduction packages on https://github.com/apmechev/GRID_LRT were deployed on the e-infrastructure by the LOFAR e-infragroup, consisting of J. B. R. Oonk (ASTRON & Leiden Observatory), A. P. Mechev (Leiden Observatory) and T. Shimwell (Leiden Observatory) with support from N. Danezi (SURFsara) and C. Schrijvers (SURFsara). This work has made use of the Dutch national e-infrastructure with the support of SURF Cooperative through grant e-infra160022.

Facilities: WSRT, LOFAR, Herschel, VLA.

REFERENCES

Anantharamaiah K. R., Payne H. E., Erickson W. C., 1988, MNRAS, 235, 151
Anantharamaiah K. R., Erickson W. C., Payne H. E., Kantharia N. G., 1994, ApJ, 430, 682
Andersson B.-G., Wannier P. G., Morris M., 1991, ApJ, 366, 464
Asgekar A. et al., 2013, A&A, 551, L11
Astropy Collaboration et al., 2013, A&A, 558, A33
Barinovs Ğ., van Hemert M. C., Krems R., Dalgarno A., 2005, ApJ, 620, 537
Batrla W., Walmsley C. M., Wilson T. L., 1984, A&A, 136, 127
Bennett C. L. et al., 1994, ApJ, 434, 587
Bialy S., Bihr S., Beuther H., Henning T., Sternberg A., 2017, ApJ, 835, 126
Bieging J. H., Crutcher R. M., 1986, ApJ, 310, 853
Bieging J. H., Goss W. M., Wilcots E. M., 1991, ApJS, 75, 999
Bihr S. et al., 2015, A&A, 580, A112
Blitz L., Williams J. P., 1999, in Lada C. J., Kylafis N. D., eds, The Origin of Stars and Planetary Systems. Kluwer Academic Publ., Netherlands, p. 3
Briggs D. S., 1995, American Astronomical Society Meeting Abstracts. p. 1444
Cazaux S., Tielens A. G. G. M., 2004, ApJ, 604, 222
Choi Y. K., Hachisuka K., Reid M. J., Xu Y., Brunthaler A., Menten K. M., Dame T. M., 2014, ApJ, 790, 99
Dame T. M., 2011, preprint (arXiv:1101.1499)
Davies R. D., Matthews H. E., 1972, MNRAS, 156, 253
De Looze I., Barlow M. J., Swinyard B. M., Rho J., Gomez H. L., Matsuura M., Wesson R., 2017, MNRAS, 465, 3309
de Oliveira-Costa A., Tegmark M., Gaensler B. M., Jonas J., Landecker T. L., Reich P., 2008, MNRAS, 388, 247
Dickey J. M., Strasser S., Gaensler B. M., Haverkorn M., Kavars D., McClure-Griffiths N. M., Stil J., Taylor A. R., 2009, ApJ, 693, 1250
Erickson W. C., McConnell D., Anantharamaiah K. R., 1995, ApJ, 454, 125
Ershov A. A., Lekht E. E., Smirnov G. T., Sorochenko R. L., 1987, Sov. Astron. Lett.,13, 8
Fanciullo L., Guillet V., Aniano G., Jones A. P., Ysard N., Miville-Deschênes M.-A., Boulanger F., Köhler M., 2015, A&A, 580, A136
Fukui Y. et al., 2009, ApJ, 705, 144
Gibson S. J., 2002, in Taylor A. R., Landecker T. L., Willis A. G., eds, ASP Conf. Ser. Vol. 276, Seeing Through the Dust: The Detection of H plbibsc-i and the Exploration of the ISM in Galaxies. Astron. Soc. Pac., San Francisco, p. 235
Goldsmith P. F., Langer W. D., Pineda J. L., Velusamy T., 2012, ApJS, 203, 13
Gong M., Ostriker E. C., Wolfire M. G., 2017, ApJ, 843, 38
Gordon M. A., Sorochenko R. L. eds, 2009, Radio Recombination Lines Astrophysics and Space Science Library, Vol. 282. Springer, Berlin
Grenier I. A., Casandjian J.-M., Terrier R., 2005, Science, 307, 1292
Gry C., Lequeux J., Boulanger F., 1992, A&A, 266, 457

Guzmán F., Badnell N. R., Williams R. J. R., van Hoof P. A. M., Chatzikos M., Ferland G. J., 2017, MNRAS, 464, 312
Habing H. J., 1968, Bull. Astron. Inst. Netherlands, 19, 421
Hayes M. A., Nussbaumer H., 1984, A&A, 134, 193
Hollenbach D. J., Tielens A. G. G. M., 1999, Rev. Mod. Phys., 71, 173
Hollenbach D., Kaufman M. J., Neufeld D., Wolfire M., Goicoechea J. R., 2012, ApJ, 754, 105
Hwang U., Laming J. M., 2012, ApJ, 746, 130
Imara N., 2015, ApJ, 803, 38
Imara N., Blitz L., 2011, ApJ, 732, 78
Kantharia N. G., Anantharamaiah K. R., 2001, J. Astrophys. Astron., 22, 51
Kantharia N. G., Anantharamaiah K. R., Payne H. E., 1998, ApJ, 506, 758
Kavars D. W., Dickey J. M., McClure-Griffiths N. M., Gaensler B. M., Green A. J., 2003, ApJ, 598, 1048
Kavars D. W., Dickey J. M., McClure-Griffiths N. M., Gaensler B. M., Green A. J., 2005, ApJ, 626, 887
Kerton C. R., 2005, ApJ, 623, 235
Kilpatrick C. D., Bieging J. H., Rieke G. H., 2014, ApJ, 796, 144
Konovalenko A. A., 1984, Sov. Astron. Lett., 10, 353
Krumholz M. R., McKee C. F., Tumlinson J., 2009, ApJ, 693, 216
Langer W. D., Penzias A. A., 1990, ApJ, 357, 477
Liszt H., Lucas R., 1999, A&A, 347, 258
Maddalena R. J., Thaddeus P., 1985, ApJ, 294, 231
McMullin J. P., Waters B., Schiebel D., Young W., Golap K., 2007, in Shaw R. A., Hill F., Bell D. J., eds, ASP. Conf. Ser. Vol. 376, Astronomical Data Analysis Software and Systems XVI. Astron. Soc. Pac., San Francisco, p. 127
Mebold U., Hills D. L., 1975, A&A, 42, 187
Megeath S. T., Allgaier E., Young E., Allen T., Pipher J. L., Wilson T. L., 2009, AJ, 137, 4072
Milam S. N., Savage C., Brewster M. A., Ziurys L. M., Wyckoff S., 2005, ApJ, 634, 1126
Mookerjea B., Kantharia N. G., Roshi D. A., Masur M., 2006, MNRAS, 371, 761
Moriarty-Schieven G. H., Wannier P. G., 1997, ApJ, 475, 642
Moss V. A., McClure-Griffiths N. M., Braun R., Hill A. S., Madsen G. J., 2012, MNRAS, 421, 3159
Motte F., Schilke P., Lis D. C., 2003, ApJ, 582, 277
Motte F. et al., 2014, A&A, 571, A32
Neufeld D. A., Wolfire M. G., Oonk J. B. R., Tielens A. G. G. M., Salas P.Radio Recombination Line Emission and Absorption in Diffuse Molecular Clouds, submitted
Nguyen Luong Q. et al., 2011, A&A, 529, A41
Oonk J. B. R. et al., 2014, MNRAS, 437, 3506
Oonk J. B. R., van Weeren R. J., Salas P., Salgado F., Morabito L. K., Toribio M. C., Tielens A. G. G. M., Röttgering H. J. A., 2017, MNRAS, 465, 1066
Pabst C. H. M. et al., 2017, A&A, 606, A29
Pascucci I., Edwards S., Heyer M., Rigliaco E., Hillenbrand L., Gorti U., Hollenbach D., Simon M. N., 2015, ApJ, 814, 14
Payne H. E., Anantharamaiah K. R., Erickson W. C., 1989, ApJ, 341, 890
Payne H. E., Anantharamaiah K. R., Erickson W. C., 1994, ApJ, 430, 690
Pineda J. L. et al., 2017, ApJ, 839, 107
Planck Collaboration XIX, 2011, A&A, 536, A19
Planck Collaboration XXIX, 2016, A&A, 586, A132
Pottasch S. R., Wesselius P. R., van Duinen R. J., 1979, A&A, 74, L15
Pound M. W., Wolfire M. G., 2008, in Argyle R. W., Bunclark P. S., Lewis J. R., eds, ASP Conf. Ser. Vol. 394, Astronomical Data Analysis Software and Systems XVII. Astron. Soc. Pac., San Francisco, p. 654
Predehl P., Schmitt J. H. M. M., 1995, A&A, 293, 889
Reed J. E., Hester J. J., Fabian A. C., Winkler P. F., 1995, ApJ, 440, 706
Roshi D. A., Kantharia N. G., 2011, MNRAS, 414, 519
Roshi D. A., Kantharia N. G., Anantharamaiah K. R., 2002, A&A, 391, 1097
Salas P. et al., 2017, MNRAS, 467, 2274
Salgado F., Morabito L. K., Oonk J. B. R., Salas P., Toribio M. C., Röttgering H. J. A., Tielens A. G. G. M., 2017a, ApJ, 837, 141
Salgado F., Morabito L. K., Oonk J. B. R., Salas P., Toribio M. C., Röttgering H. J. A., Tielens A. G. G. M., 2017b, ApJ, 837, 142
Schwarz U. J., Goss W. M., Kalberla P. M. W., 1997, A&AS, 123
Shaver P. A., 1975, Pramana, 5, 1
Sofia U. J., Cardelli J. A., Guerin K. P., Meyer D. M., 1997, ApJ, 482, L105
Sorochenko R. L., Smirnov G. T., 2010, Astron. Rep., 54, 776
Sorochenko R. L., Walmsley C. M., 1991, Astron. Astrophys. Trans.1, 31
Stanimirović S., Murray C. E., Lee M.-Y., Heiles C., Miller J., 2014, ApJ, 793, 132
Stepkin S. V., Konovalenko A. A., Kantharia N. G., Udaya Shankar N., 2007, MNRAS, 374, 852
Sternberg A., Le Petit F., Roueff E., Le Bourlot J., 2014, ApJ, 790, 10
Tielens A. G. G. M., Hollenbach D., 1985, ApJ, 291, 722
Troland T. H., Crutcher R. M., Heiles C., 1985, ApJ, 298, 808
van Gorkom J. H., Ekers R. D., 1989, in Perley R. A., Schwab F. R., Bridle A. H., eds, ASP Conf. Ser. Vol. 6, Synthesis Imaging in Radio Astronomy. Astron. Soc. Pac., San Francisco, p. 341
van Haarlem M. P. et al., 2013, A&A, 556, A2
van Langevelde H. J., Cotton W. D., 1990, A&A, 239, L5
Vrinceanu D., Onofrio R., Sadeghpour H. R., 2012, ApJ, 747, 56
Vrinceanu D., Onofrio R., Sadeghpour H. R., 2017, MNRAS, 471, 3051
Watson W. D., Western L. R., Christensen R. B., 1980, ApJ, 240, 956
Williams J. P., Maddalena R. J., 1996, ApJ, 464, 247
Wilson N. J., Bell K. L., 2002, MNRAS, 337, 1027
Wilson T. L., Mauersberger R., Muders D., Przewodnik A., Olano C. A., 1993, A&A, 280, 221
Wolfire M. G., Hollenbach D., McKee C. F., Tielens A. G. G. M., Bakes E. L. O., 1995, ApJ, 443, 152
Wolfire M. G., McKee C. F., Hollenbach D., Tielens A. G. G. M., 2003, ApJ, 587, 278
Wolfire M. G., Hollenbach D., McKee C. F., 2010, ApJ, 716, 1191
Xu Y., Reid M. J., Zheng X. W., Menten K. M., 2006, Science, 311, 54
Zheng H. et al., 2017, MNRAS, 464, 3486
Zhu H., Tian W., Li A., Zhang M., 2017, MNRAS, 471, 3494

This paper has been typeset from a TEX/LATEX file prepared by the author.